



저작자표시-비영리-변경금지 2.0 대한민국

이용자는 아래의 조건을 따르는 경우에 한하여 자유롭게

- 이 저작물을 복제, 배포, 전송, 전시, 공연 및 방송할 수 있습니다.

다음과 같은 조건을 따라야 합니다:



저작자표시. 귀하는 원저작자를 표시하여야 합니다.



비영리. 귀하는 이 저작물을 영리 목적으로 이용할 수 없습니다.



변경금지. 귀하는 이 저작물을 개작, 변형 또는 가공할 수 없습니다.

- 귀하는, 이 저작물의 재이용이나 배포의 경우, 이 저작물에 적용된 이용허락조건을 명확하게 나타내어야 합니다.
- 저작권자로부터 별도의 허가를 받으면 이러한 조건들은 적용되지 않습니다.

저작권법에 따른 이용자의 권리는 위의 내용에 의하여 영향을 받지 않습니다.

이것은 [이용허락규약\(Legal Code\)](#)을 이해하기 쉽게 요약한 것입니다.

[Disclaimer](#)

공학석사 학위논문

Estimation of joint roughness
coefficient of rock exposure
using terrestrial laser scanner
and artificial neural network

지상레이저스캐너와 인공신경망을 이용한
암반 노출면의 절리 거칠기 지수 측정

2023 년 2 월

서울대학교 대학원

에너지시스템공학부

이 승 원

Estimation of joint roughness coefficient of rock exposure using terrestrial laser scanner and artificial neural network

지도 교수 전 석 원

이 논문을 공학석사 학위논문으로 제출함
2023 년 2 월

서울대학교 대학원
에너지시스템공학부
이 승 원

이승원의 공학석사 학위논문을 인준함
2023 년 2 월

위 원 장 _____ 송 재 준 _____ (인)

부위원장 _____ 전 석 원 _____ (인)

위 원 _____ 민 기 복 _____ (인)

Abstract

Estimation of joint roughness coefficient of rock exposure using terrestrial laser scanner and artificial neural network

Seungwon Lee

Department of Energy Systems Engineering

The Graduate School

Seoul National University

Joint Roughness Coefficient (JRC) is a parameter representing degree of roughness of rock discontinuities in Barton–Bandis joint model. It can be measured by visual comparison between roughness profiles acquired from target discontinuities and the reference profiles. Although performing this method is much convenient than lab or field tests on joint specimens, it can be time-consuming and unsafe. In this thesis, a method to estimate JRC using Terrestrial Laser Scanner (TLS) is suggested for quick and safe assessment of JRC. After obtaining 3D point cloud of rock exposure in distance, JRC of discontinuities on it is estimated.

According to several previous works, measuring small-scale roughness using TLS scan data is challenging due to noise existent in it. The strategy used in this thesis is to employ an ANN for 3D point clouds. The ANN can receive point clouds of discontinuities as input and output their JRC. By training the ANN with a number of point clouds containing TLS noise, it was expected that the ANN can learn how to estimate their JRC regardless of the existence of noise. Since it is not attainable to make a real dataset, point

clouds of synthetic rough surfaces are generated using a fractal based algorithm instead of real TLS scan data. Each surface is labeled with its JRC, and TLS noise is artificially applied on it to imitate actual TLS scan data. After being trained with the synthetic training dataset, the ANN is tested on joint surfaces on actual TLS scan data. It is shown that the trained ANN can estimate JRC of the joint surfaces regardless of noise level of TLS scan data while an existing method does not work well on data with larger noise level. In addition, methods to deal with scale effect of JRC are also introduced.

Keywords: Joint roughness coefficient, Terrestrial laser scanner, Artificial neural network, Rock, Point cloud, LiDAR

Student Number: 2021–26971

Contents

Chapter 1. Introduction	1
1.1. Motivation	1
1.2. Agendas and overview	3
 Chapter 2. Measuring JRC of 3D point clouds	 5
2.1. Joint roughness coefficient	5
2.2. JRC calculation using digitized data of surface geometry	10
2.3. Issues relevant to JRC	15
2.4. Synthetic surface generation	20
2.5. Calculating JRC of the generated surfaces	23
 Chapter 3. TLS precision.....	 25
3.1. Basics of TLS	25
3.2. Factors disturbing TLS precision	30
3.3. Measuring roughness of joint using TLS	31
3.4. Range and angular noise	33
3.5. Mixed-pixel effect	36
3.6. Synthetic noise application.....	42
3.7. Training data generation	49
 Chapter 4. ANN estimating JRC of TLS data.....	 52
4.1. PointNet	52
4.2. Test data acquisition.....	54
4.3. Training procedure	61
4.4. Test results and comparative analysis	62
4.5. How to deal with scale effect.....	66

Chapter 5. Conclusion	68
References	71
Appendix A. Figures of test data	78
Appendix B. Large scale roughness profiles	83
Abstract in Korean.....	86

List of Tables

Table 3–1. Technical specifications of Faro Focus S 350+ and S 350 (Faro, 2021).	29
Table 4–1. Incidence angle and distance of surfaces from Faro Focus S 350+. Index of each surface is shown in Fig. A–1, Appendix A.	60
Table 4–2. JRCn estimated with two different methods.	67
Table A–1. 3D plot of test data shown in Fig. A–1. First, second and third column represent data index, corresponding data scanned by Faro Focus S 350+ and corresponding data scanned by Faro Focus S 350, respectively. Here, point cloud from Faro Focus S 350 did not contain surface #2. Digits in the plots are in centimeter unit.	78
Table B–1. Plots of roughness profiles in Fig. B–1. First column represents the index. Digits in the plots are in meter unit.	83

List of Figures

Figure 1–1. Acquisition of roughness profile using Barton comb (Barton and Choubey, 1977).....	2
Figure 2–1. Barton’s reference profiles (Barton and Choubey, 1977).....	8
Figure 2–2. (a) Suggested coordinates of (displacement, JRCmob/JRC) and (b) examples of shear strength–displacement and dilation–displacement curves plotted using the coordinates with different input parameters (Barton and Bandis, 2017).....	9
Figure 2–3. Digitization of a roughness profile (Kulatilake et al., 1995).	10
Figure 2–4. Iteration process of Koch snowflake (Mandelbrot, 1982). ...	12
Figure 2–5. Potential contact area with respect to minimum apparent dip angle (Grasselli and Egger, 2003).....	13
Figure 2–6. Scale effect on three main components constructing the shear strength of rock joints (Bandis et al., 1981).	16
Figure 2–7. Reduction curves with respect to joint length for JCS and JRC. Nomenclatures for the parameters in the axes are described in the text (Bandis et al., 1981).....	17
Figure 2–8. Illustrations of the a/L method (amplitude–length method) for estimating the large–scale JRC (Barton and Bandis, 2017)...	18
Figure 2–9. Erasure of features smaller than a pin diameter (Tatone and Grasselli, 2010).	20
Figure 2–10. PSD of a joint profile (Carr and Warriner, 1989).....	21
Figure 2–11. Synthetic rough surfaces generated by the algorithm. All three surfaces have the same JRC of 10 but different H. From the left, H is equal to 0.5, 0.7 and 0.9, respectively.	22
Figure 2–12. Generated surfaces with roughness anisotropy.	22
Figure 2–13. Rough profile from a generated surface (top) and the same	

profile after applying Barton comb (bottom). Digits in axes are in cm unit.....	24
Figure 3–1. (a) TLS outlook (Faro Focus S 350+) and (b) rotating direction (horizontal/vertical) of the laser beam (Muralikrishnan, 2021).	26
Figure 3–2. Polar coordinates of a detected target point. R, Φ and θ denote the range, vertical angle and horizontal angle, respectively...	27
Figure 3–3. Difference between accuracy and precision (Soudarissanane, 2016).	30
Figure 3–4. Schematic images showing the process of roughness estimation by stereonet projection (Kemeny and Turner, 2008).....	32
Figure 3–5. (a): Divergence of laser beam. (b): Laser beam falling on a surface edge. (c): Mixed–pixels in a point cloud. Different types of mixed–pixels can be made depending on the range difference between foreground and background (a, b: Reshetyuk, 2009, c: Wang et al., 2016).....	36
Figure 3–6. Irradiance distribution in the cross–section of a Gaussian beam (Reshetyuk, 2009).....	37
Figure 3–7. Light reflected from a Lambertian reflector has the same radiance regardless of the angle from the normal. Yellow arrows represent the intensity magnitude of the reflected light while red and blue arrows represent the surface normal and an arbitrary direction, respectively (After Photonik and Sandner, 2015)..	39
Figure 3–8. Determining the influencing area by setting the boundary....	44
Figure 3–9. Normal vectors of all the points inside a beam area. Black thorns indicate the normal vectors.....	47
Figure 3–10. Point cloud of a rough surface whose JRCx is 19.13 (left). And the same surface after adding the mixed–pixel effect (right). TLS	

10 m away in z-axis direction was assumed in this case.	48
Figure 3-11. One of the training data. JRCx of this surface is 18.98.....	50
Figure 4-1. PointNet structure (Qi et al., 2017).	53
Figure 4-2. Picture of (a) granite rock exposure and target surfaces framed by white papers, and (b) scanning configuration.....	55
Figure 4-3. Six roughness profiles acquired from a surface. Index of the surfaces are shown in Appendix A, Fig. A-1.....	56
Figure 4-4. Point cloud of the outcrop visualized by CloudCompare.....	57
Figure 4-5. Matching two different point clouds of the same object. (a): Point cloud from Faro Focus S 350, (b): Point cloud from Faro Focus S 350+, (c): (a) and (b) after registration using ICP, (d): Remaining point clouds after the targets were cropped.	58
Figure 4-6. Line drawn to be parallel to a side of the surface.	59
Figure 4-7. Acquisition of roughness profile from TLS scan data using existing method used in Kemeny and Turner (2008) and Marsch et al. (2020).....	62
Figure 4-8. Results of the JRCx measurement on test dataset using the existing method. Left figure shows the result on surfaces from Faro Focus S 350+, and right one shows the result on surfaces from Faro Focus S 350. Horizontal and vertical axes of each figure represent model's JRCx prediction and hand-measured JRCx, respectively.	63
Figure 4-9. Results of the ANN's JRCx estimation on test dataset.	63
Figure A-1. Index of test data.	78
Figure B-1. Index of the profiles... ..	83

Chapter 1. Introduction

1.1. Motivation

We need to know shear strength of discontinuities in a rock mass to analyze its mechanical stability and there are several ways for it. For example, we can perform direct shear tests on rock samples containing the discontinuities. But it is sometimes difficult to take the samples because of economic reasons or inaccessibility. On the other hand, we can use existing equations to predict the shear strength. In this way, we can just measure parameters constructing the equation instead of conducting the direct shear test.

Barton–Bandis shear criterion is the most widely used approach to predict shear strength of discontinuities (Tatone and Grasselli, 2010). According to the criterion, factors that affect peak shear strength are joint roughness, joint wall strength, magnitude of normal stress and residual friction angle. In this criterion, joint roughness is quantified with a parameter named Joint Roughness Coefficient (JRC) and we can carry out direct shear test, pull test, tilt test and visual comparison to measure it. Except for the last one, samples containing the discontinuity are required, and those having small size and large JRC cannot be determined by pull or tilt test due to the limit of normal load (Barton and Choubey, 1977).

The most convenient and widely used method is visual comparison, which is to get JRC only by observing surface morphology of discontinuities on rock exposure. Measurers obtain roughness profiles from the surfaces using a device called Barton comb (Fig. 1–1) and compare them with ten reference profiles provided in Barton and Choubey (1977). Since JRC ranges where the reference profiles belong to are suggested in a table, they can assign

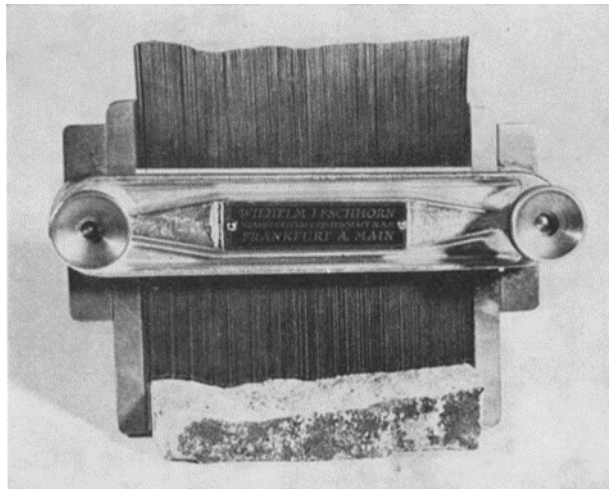


Figure 1–1. Acquisition of roughness profile using Barton comb (Barton and Choubey, 1977).

JRC of each obtained profile by choosing a reference profile which has the most similar degree of roughness.

However, there can be some difficulties of conducting visual comparison. It might take much time as measurers have to acquire several profiles for a single surface since JRC has deviation within a surface. Also, unreachable part of a rock mass cannot be inspected and risks of rockfall exist during the measurement. In addition, the assigned JRC values may vary depending on the measurer' s consistency.

To overcome those obstacles, using a remote 3D laser scanner can be considered. LiDAR (Light Detection and Ranging) is the popular term referring to both the device itself and relevant techniques. The device enables obtaining point cloud of surrounding area with high resolution and short time by using laser. Terrestrial Laser Scanner (TLS) is a type of LiDAR device which is installed on the ground above a tripod to scan the whole surrounding area. Surfaces that are several to several hundred meters away from the device can be scanned and thus, we can scan rock exposures that are inaccessible and get their point cloud quickly using a TLS. These advantages drove lots of rock engineers to use it for various purposes

including roughness measurement (Feng and Röshoff, 2015).

Several works have been done on roughness characterization of rock using TLS and their authors said that it is difficult or even not possible to measure small-scale roughness due to the existence of noise in TLS scan data (Fardin et al., 2004; Kemeny and Turner, 2008; Gigli and Casagli, 2011; Bitenc et al., 2019; Marsch et al., 2020). In this context, if we can make a noise-independent estimator which can predict JRC of discontinuities on TLS scan data with consistent judgement, all the problems mentioned above will be resolved reasonably.

1.2. Agendas and overview

Main objective of this thesis is to develop a JRC estimator for the point cloud of rock discontinuities on TLS scan data in order to save time and labors consumed for the measurement. To achieve that goal, Artificial Neural Network (ANN) is employed to be the estimator that excludes human bias and makes consistent judgement regardless of the existence of noise in TLS data.

However, large amount of data is required to train an ANN. In other words, a number of rock discontinuities with various characteristics (e.g. roughness, rock type) have to be scanned with TLS. In addition, all the data should be labeled with consistency for training. Considering the amount of data, it would be better to find an automatic way to label them. In this thesis, synthetic point clouds of rough surfaces with various characteristics are generated using an algorithm instead of real scan data to fill the need of big data, and their JRC is computed with a simple mathematical method.

There is another problem that the synthetic surfaces do not contain noises

existing in TLS scan data. Therefore, artificial noises are applied on the synthetic data and the ANN is trained with the noise–applied data so that it can learn how to deal with the noise.

In Chapter 2, utility of JRC in Barton–Bandis joint model and methods to measure JRC consistently are explained. Also, some issues including roughness anisotropy and scale effect are dealt with and the algorithmic way to generate and process the training data is illustrated.

In Chapter 3, basics of TLS and its noise sources are explained, and the algorithmic procedure to put artificial noises on the training data are introduced.

In Chapter 4, an ANN named PointNet is trained to estimate JRC with the synthetic training dataset and validated with true TLS data.

In Chapter 5, summary, contributions and limitations of this thesis are suggested in conclusion.

Chapter 2. Measuring JRC of 3D point clouds

Roughness is an important property of rock discontinuities in hydro-mechanical perspective, and JRC is the most widely used description of roughness (Barton et al., 1985; Tatone and Grasselli, 2010). Barton and Choubey (1977) suggested a method to estimate JRC only by using geometric features of rock surfaces without conducting any mechanical experiments. Since this method largely depends on human determination, it is rather subjective (Barton and Bandis, 2017). Thus, more precise and consistent ways to calculate JRC have been suggested by many authors. Topics of this kind together with the utility of JRC are dealt with in the early part of this chapter.

Fractal models have been employed to imitate rough rock surfaces in previous works combined with numerical simulation and 3D printing techniques (Brown, 1987; Fereshtenejad et al., 2021). An algorithm generating random fractal surfaces is utilized in this thesis to make large amount of data needed for training an ANN. Therefore, relevant principles and the procedure are shown in the rest part of this chapter.

2.1. Joint roughness coefficient

Barton and Choubey (1977) suggested an empirical equation to predict peak shear strength of unfilled discontinuities, which is,

$$\tau = \sigma_n \tan \left[\text{JRC} \log_{10} \frac{\text{JCS}}{\sigma_n} + \varphi_r \right] \quad (2-1)$$

where τ , σ_n , JCS and φ_r are peak shear strength of the discontinuity, normal stress, Joint wall Compressive Strength and residual friction angle, respectively. Here, the term joint is used to describe all natural discontinuities having zero tensile strength, no soft infilling and no previous history of displacements (Bandis et al., 1981). From the equation, we can infer that the peak shear strength of a discontinuity increases as it gets rougher and the asperities get stronger. Also, when the normal stress acting on it is high, it is easy to break the asperities so that their contribution on shear strength diminishes.

To use Eq. (2-1) for prediction, each parameter has to be measured. If the joint is dry and unweathered, its JCS and residual friction angle are equal to the uniaxial compressive strength and basic friction angle, respectively. Otherwise, they can be estimated using a Schmidt hammer. In order to get JRC, several methods such as direct shear test, pull test, tilt test and visual comparison can be performed. In this thesis, only methods for measuring JRC are explained, so please refer to Barton and Choubey (1977) for further information on the measurement of JCS and residual friction angle.

By carrying out the direct shear test on a joint specimen under certain normal load, peak shear strength of the joint is obtained. Then, its JRC can be back-calculated using Eq. (2-2) which is the rearranged form of Eq. (2-1).

$$JRC = \frac{\arctan\left[\frac{\tau}{\sigma_n}\right] - \varphi_r}{\log_{10} \frac{JCS}{\sigma_n}} \quad (2-2)$$

Alternatively, push or pull test can be performed, which is shear test that only uses self-weight of the upper specimen as normal load. Same with direct shear test, Eq. (2-2) is used to calculate JRC in this case.

Tilt test is another way to use only the self-weight. It is a method where the joint sample is tilted slowly until the upper part starts to slide. By measuring the angle of inclination which corresponds to $\arctan[\tau/\sigma_n]$ in Eq. (2-2), we can calculate JRC using the equation. Here, Barton and Choubey (1977) used Eq. (2-3) to calculate σ_n in Eq. (2-2) since small joint samples tend to have stress concentration due to torque.

$$\sigma_n = \gamma h \cos^2 \alpha \quad (2-3)$$

where γ , h and α represent density, height of the sample and angle of inclination, respectively. Also, small sample tends to be toppled before sliding when it has JRC higher than 8.

The most convenient way to estimate the full range of JRC (0 to 20) of discontinuities is to observe their roughness profiles visually. Barton and Choubey (1977) conducted direct shear tests on 136 different joint samples and back-calculated their JRC. After that, they divided JRC into 10 ranges and suggested a profile that is the most representative for each JRC range as Fig. 2-1. Using the Barton comb and this figure, measurers can get profiles of discontinuities and assign their JRC range by comparing them with the reference profiles.

Parameters in Eq. (2-1) (JRC, JCS, ϕ_r) can be used to estimate not only the peak shear strength of discontinuities, but also shear displacement at

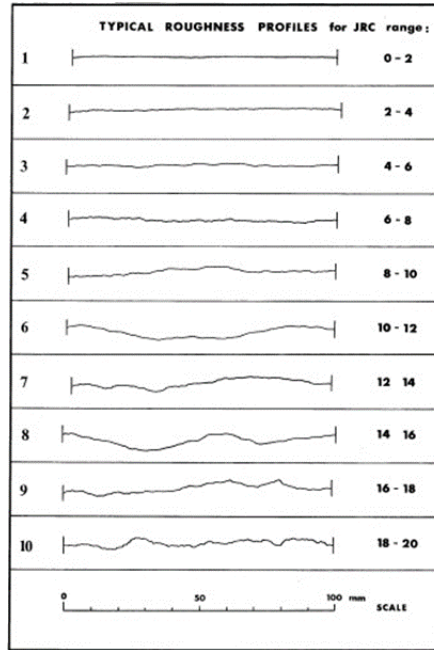


Figure 2-1. Barton's reference profiles (Barton and Choubey, 1977).

peak shear strength (δ (peak)), peak dilation angle (d_n). Equations for those estimations are as follows:

$$\delta \text{ (peak)} = \frac{L}{500} \left[\frac{\text{JRC}}{L} \right]^{0.33} \quad (\text{Barton, 1982a}) \quad (2-4)$$

$$d_n = \frac{1}{2} \text{JRC} \log_{10} \frac{\text{JCS}}{\sigma_n} \quad (\text{Barton and Choubey, 1977}) \quad (2-5)$$

where L represents length of the joint in meter unit.

In addition, Barton (1982a) modeled the pre- and post-peak of shear strength and dilation by introducing the concept of mobilized JRC (JRC_{mob}). This concept is based on the assumption that the degree of mobilized roughness is the only variable changing during shear in Eq. (2-1) and (2-5). By suggesting the realistic coordinates of JRC_{mob} over peak JRC versus

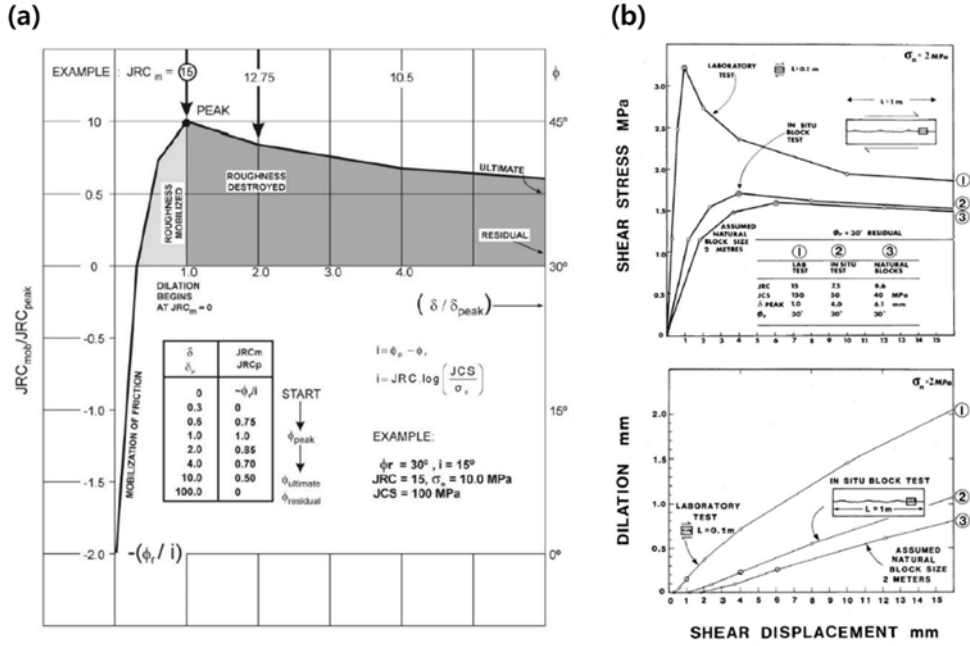


Figure 2–2. (a) Suggested coordinates of (displacement, JRC_{mob}/JRC) and (b) examples of shear strength–displacement and dilation–displacement curves plotted using the coordinates with different input parameters (Barton and Bandis, 2017).

displacement over δ (peak) as shown in Fig. 2–2(a), mobilized shear strength (τ_{mob}) and dilation can be plotted with respect to displacement using following equations:

$$\tau_{mob} = \sigma_n \tan \left[JRC_{mob} \log_{10} \frac{JCS}{\sigma_n} + \phi_r \right] \quad (2-6)$$

$$d_{n, mob} = \frac{1}{2} JRC_{mob} \log_{10} \frac{JCS}{\sigma_n} \quad (2-7)$$

Examples of the plots are shown in Fig. 2–2(b). Also, please refer to Barton (1982a) and Barton et al. (1985) for comprehensive descriptions on utility of JRC in Barton–Bandis joint model.

2.2. JRC calculation using digitized data of surface geometry

1) Statistical parameters

Many researchers tried to measure JRC of roughness profiles precisely and consistently using statistical parameters rather than visual comparison. The most widely used parameter is Z_2 in Tse and Cruden (1979) (Jang et al., 2014). The authors plotted the reference profiles of Fig. 2-1 on xy-plane and align their shear direction to be the x-axis direction. After that, they digitized the profiles by sampling their amplitude (y-coordinates) at equal x-intervals as shown in Fig. 2-3 and calculated Z_2 of each profile using the following equation:

$$Z_2 = \left[\frac{1}{L} \sum_{i=1}^{n-1} \frac{(y_{i+1} - y_i)^2}{\Delta x} \right]^{1/2} \quad (2-8)$$

where L , y_i and Δx denote profile length, y-coordinate of i-th sample and size of x-interval, respectively. Using the back-calculated JRC of each reference profile written in Barton and Choubey (1977) and regression

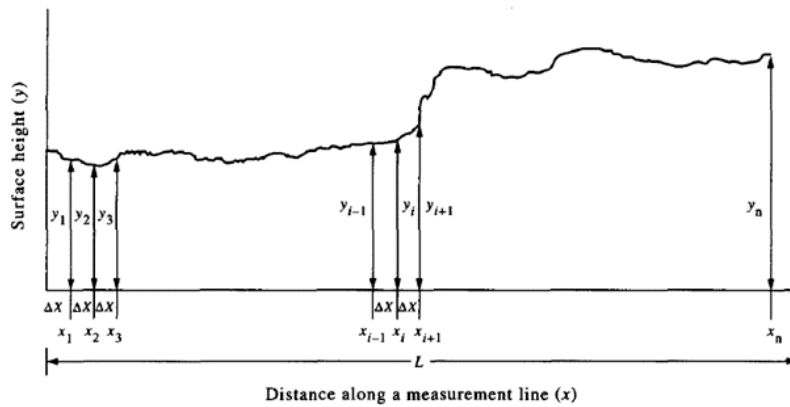


Figure 2-3. Digitization of a roughness profile (Kulatilake et al., 1995).

analysis, they derived a relationship between Z_2 and JRC as follow:

$$\text{JRC} = 32.2 + 32.47 \log Z_2 \quad (2-9)$$

Similarly, several other statistical parameters have been suggested to calculate JRC as follows:

$$\text{SF} = \frac{1}{L} \sum_{i=1}^{n-1} (y_{i+1} - y_i)^2 \Delta x \quad (\text{Tse and Cruden, 1979}) \quad (2-10)$$

$$R_p = \frac{\sum_{i=1}^{n-1} [\Delta x^2 + (y_{i+1} - y_i)^2]^{1/2}}{L} \quad (\text{Maerz et al., 1990}) \quad (2-11)$$

2) Fractal dimension

Otherwise, there is another way of calculating JRC using fractal parameters. Fractals are, in short, geometries having constant degree of irregularity at all scales (Mandelbrot, 1982). For instance, Fig. 2-4 shows the iteration process of a representative fractal geometry called Koch snowflake. In each iteration, every side of the geometry is trisected and the middle segment is substituted by two other segments of equal length so as to the total length becomes 4/3 times the length of previous stage. If this process continues infinitely, same degree of irregularity will be observed even though the geometry is enlarged.

Fractals are classified into two types, self-similar fractals and self-affine fractals. Self-similar fractals refer to geometries where the degree of irregularity holds regardless of enlarging it (e.g. Koch snowflake). On the



Figure 2–4. Iteration process of Koch snowflake (Mandelbrot, 1982).

other hand, self-affine fractals must be scaled differently in different directions to maintain their degree of irregularity. For example, if a function of a self-affine fractal, $y=f(x)$, is scale k times in x -axis direction, it should be scaled k^H times in y -axis direction to have the same degree of irregularity. Here, H is a parameter called Hurst exponent, which is expressed as a number between 0 and 1. Thinking of this example, we can imagine that a fractal will get rougher as it is enlarged when it has small H . There is another fractal parameter called fractal dimension, D , which has relationship with H as below (Jacobs et al., 2017; Odling, 1994):

$$D = \begin{cases} 2 - H & \text{(for curves)} \\ 3 - H & \text{(for surfaces)} \end{cases} \quad (2-12)$$

Several researchers have stated that the rock surfaces have characteristics of self-affine fractals and calculated their fractal dimensions to quantify their roughness. They employed various approaches such as divider method, box-counting method, Power Spectral Density (PSD) method and variogram method to get fractal dimension of self-affine curves (Carr and Warriner, 1989; Huang et al., 1992; Kulatilake and Um, 1999; Lee et al., 1990; Odling,

1994). Based on the range of fractal dimension of various joint surfaces obtained from previous works, some researchers mentioned that rock discontinuities usually have the Hurst exponents between 0.5 and 1 (Huang et al., 1992; Odling, 1994). In addition, relationships between fractal dimension of the roughness profile and JRC have been suggested (Carr and Warriner, 1989; Lee et al., 1990).

3) Grasselli parameter

As another method to quantify joint roughness, Tatone and Grasselli (2009) suggested a roughness parameter, $\theta_{\max}^*/(C+1)$, that can be measured from 3D data of joint surfaces to characterize their roughness in all directions, where variables comprising the parameter had been introduced in Grasselli and Egger (2003).

Grasselli and Egger (2003) assumed that inclination angle of asperities in joint surfaces determine contact area during shear so that it affects the

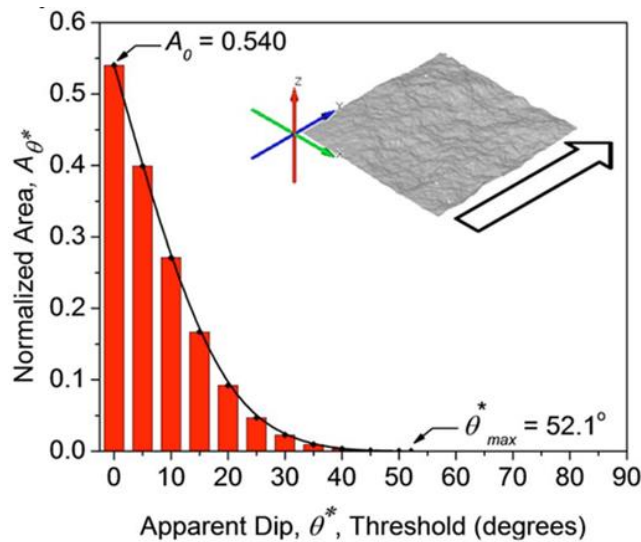


Figure 2–5. Potential contact area with respect to minimum apparent dip angle (Grasselli and Egger, 2003).

shear strength. They digitized target surfaces into 3D meshes and calculated the area and dip angle in shear direction of each mesh. After that, total area of meshes having dip angle larger than certain threshold dip angle was calculated and plotted against the threshold dip angle as shown in Fig. 2–5. Then, following equation was fit to the plot:

$$A_{\theta^*} = A_0 \left(\frac{\theta_{\max}^* - \theta^*}{\theta_{\max}^*} \right)^c \quad (2-13)$$

where A_0 , θ^* , θ_{\max}^* , A_{θ^*} and c represent the total area of meshes having dip angle larger than 0, threshold dip angle, maximum apparent dip angle, area of meshes having dip angle larger than θ^* and dimensionless fitting parameter, respectively.

Tatone and Grasselli (2009) suggested $\theta_{\max}^*/(C+1)$ consisting of the parameters in Eq. (2–13) as a roughness parameter for 3D joint surface. Using this parameter, they were able to characterize and visualize roughness anisotropy of discontinuities. Additionally, Tatone and Grasselli (2010) introduced 2D version of the parameter, $\theta_{\max}^*/(C+1)_{2D}$, which is applicable on 2D roughness profiles. By calculating the parameter of the Barton's reference profiles, they obtained the relationship between $\theta_{\max}^*/(C+1)_{2D}$ and JRC.

So far, parameters for roughness quantification were shortly explained. In this thesis, Z_2 –JRC relationship will be used for the following reasons:

- ① Z_2 is easy to calculate and it is one of the most popular parameters for

calculating JRC.

- ② The process of calculating the fractal dimension has many variables to consider and there are different opinions about the optimal values of the variables (e.g. the suitable range of dividers in Kulatilake et al., 1997 and Jang et al., 2014). In addition, curve-fitting procedure is required to calculate the parameter in some cases, which makes labeling the large amount of data difficult.
- ③ Grasselli parameter has an advantage to characterize roughness in all directions. But that advantage diminishes when it is used for calculating JRC since JRC itself does not contain any directional information. Also, curve-fitting procedure is required to get C in Eq. (2-13).

2.3. Issues relevant to JRC

1) Scale effect

Bandis et al. (1981) pointed out that the peak shear strength of discontinuities decreases as its size gets larger due to the existence of scale effect on JCS and JRC. According to the authors, the shear strength consists of three components which are asperity failure component, geometrical component and residual frictional component (Fig. 2-6). Among those, only residual frictional component remains constant regardless of the size of the joint while the effect of the others diminishes as the joint gets larger.

Conducting lots of experimental results, the authors found out that the number of small contact areas during shear increases in small joints than large joints while the size of individual contact areas decreases. Based on these results, it can be thought that the increased amount of mobilized asperities in large joint leads to the inclusion of more defects (e.g. micro-

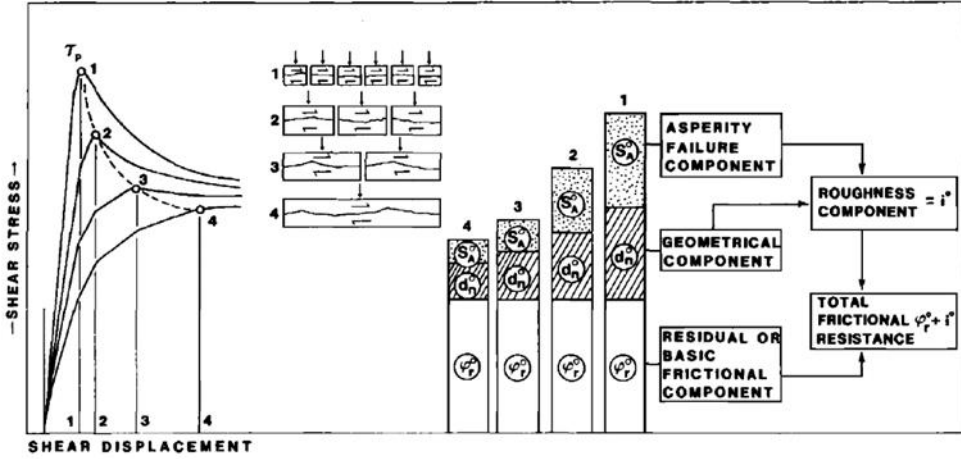


Figure 2-6. Scale effect on three main components constructing the shear strength of rock joints (Bandis et al., 1981).

cracks) during shear so that causes the degradation of JCS. Also, it was observed that the peak dilation angle decreases as the joint size increases. It was interpreted as the base-length of mobilized asperities gets longer as the joint gets larger, which leads to decline of JRC.

By using the residual friction angle and measuring the dilation angle and peak shear strength, the authors were able to separate the effect of each component in Fig. 2-6. As a result, the authors suggested reduction curves with respect to the size of joint for JCS and JRC as shown in Fig. 2-7. Also, Barton (1982a) derived equations for the curves as follows:

$$JCS_n \cong JCS_0 \left(\frac{L_n}{L_0} \right)^{-0.03JRC_0} \quad (2-14)$$

$$JRC_n \cong JRC_0 \left(\frac{L_n}{L_0} \right)^{-0.02JRC_0} \quad (2-15)$$

In these equations, L_0 represents the lab-scale joint length (10 cm) and

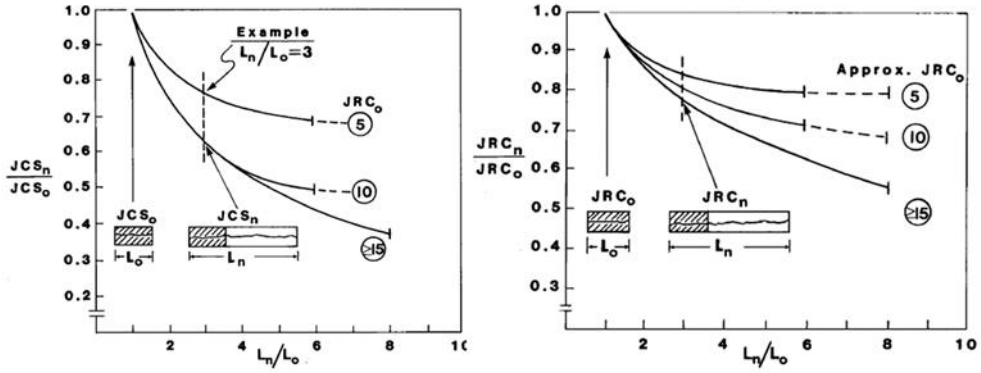


Figure 2-7. Reduction curves with respect to joint length for JCS and JRC. Nomenclatures for the parameters in the axes are described in the text (Bandis et al., 1981).

JCS_0 and JRC_0 are JCS and JRC of joint having length L_0 . In the same way, L_n represents the joint length of interest and JCS_n and JRC_n denote JCS and JRC of joint having length L_n . By using these equations, we can estimate JCS and JRC of joint with different lengths using the measured values of JCS and JRC of joint with 10 cm length.

However, Eq. (2-15) does not work well on joint samples with dissimilar roughness on small and large scales (Bandis et al., 1981). That is, a joint can be rough on small scale while planar on large scale, or conversely, it can be smooth on small scale while quite undulating on large scale (Barton, 1982b). Therefore, Barton (1982b) suggested an alternative method to estimate JRC by measuring the maximum amplitude (a) over a joint length (L) using a straight edge as shown in Fig. 2-8 with the below equations:

$$JRC \cong \begin{cases} 400 a/L & (L = 0.1 \text{ m}) \\ 450 a/L & (L = 1.0 \text{ m}) \\ 500 a/L & (L = 10 \text{ m}) \end{cases} \quad (2-16)$$

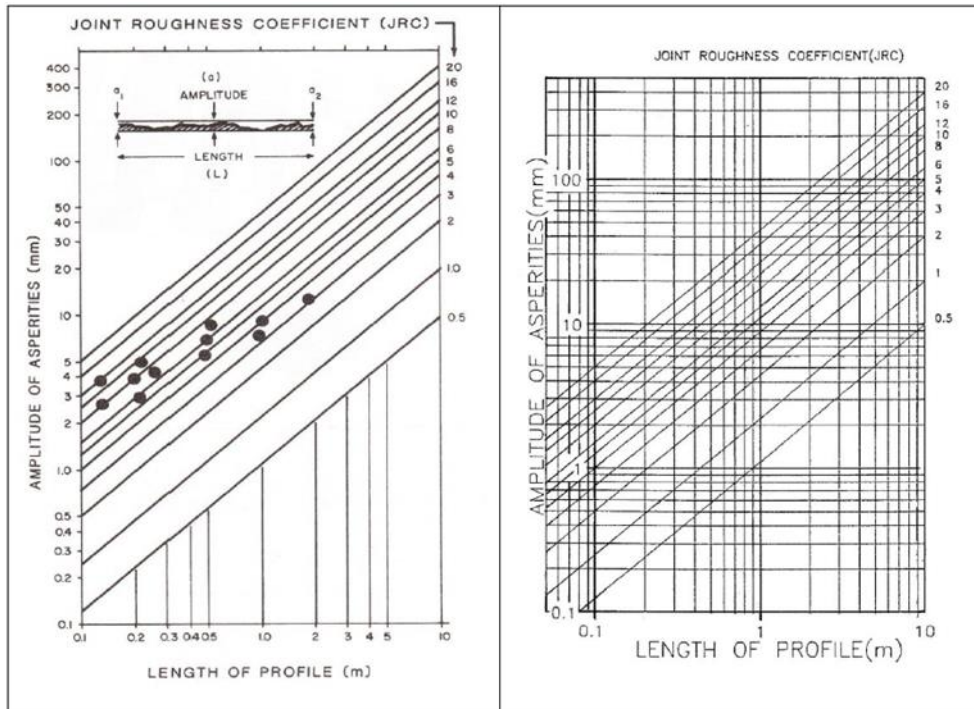


Figure 2–8. Illustrations of the a/L method (amplitude–length method) for estimating the large–scale JRC (Barton and Bandis, 2017).

Barton (1982b) recommended to utilize the JRC estimating methods concurrently as many as possible to improve reliability:

- ① Tilt tests on joints sampled in drillcore and to use Eq. (2–15).
- ② Tilt tests on blocks of natural size.
- ③ Roughness profiling at different scales and using Fig. 2–8 or Eq. (2–16) to scale JRC.

Given that the Cartesian coordinates of joint surfaces are the only available data from TLS scanning, following methods can be considered to be used concurrently when we measure JRC using TLS without mechanical tests:

- ① Visual comparison using Fig. 2–1 and scaling the JRC with respect to the joint size using Eq. (2–15).
- ② Roughness profiling at different scales and using Fig. 2–8 or Eq. (2–

16).

2) Anisotropy

Degree of roughness is different with respect to the direction in the joint surfaces, which leads to anisotropy of the shear strength. So, it is important to measure roughness in the potential shear direction. For instance, shearing usually occurs in the dip direction in a single joint and in the case of two intersecting joints, the potential shear direction would be parallel to the intersection (ISRM, 1978). Otherwise if the direction of sliding is unknown, ISRM (1978) said roughness must be sampled in three dimensions instead of two.

3) Dependence on sampling interval and resolution of device

Yu and Vayssade (1991) discussed about a problem that Z_2 value of a profile varies sensitively as sampling interval, Δx in Eq. (2-8), changes. Pointing out that Tse and Cruden (1979) had used 0.5 mm as the sampling interval to gain relationship between Z_2 and JRC (Eq. 2-9), they suggested new Z_2 -JRC relationships with three different sampling intervals:

$$\text{JRC} = \begin{cases} 60.32 Z_2 - 4.51 & (\Delta x = 0.25 \text{ mm}) \\ 61.79 Z_2 - 3.47 & (\Delta x = 0.50 \text{ mm}) \\ 64.22 Z_2 - 2.31 & (\Delta x = 1 \text{ mm}) \end{cases} \quad (2-17)$$

Tatone (2009) and Tatone and Grasselli (2010) discussed some issues regarding resolution of instrument for roughness measurement. They mentioned that when we use the Barton comb to obtain roughness profiles,

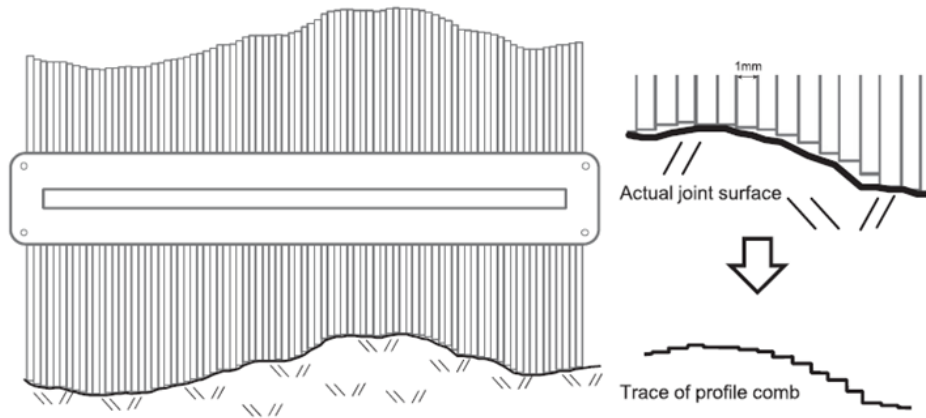


Figure 2–9. Erasure of features smaller than a pin diameter (Tatone and Grasselli, 2010).

rough features smaller than a pin diameter of the comb are ignored. As the original reference profiles in Fig. 2–1 were obtained with the Barton comb, they do not carry any rough features smaller than the pin size. Therefore, using sampling interval smaller than the pin size for calculating JRC by Z_2 or any other parameters will not produce any additional information about roughness, leading to the inclusion of step–like features introduced by the pin geometry as shown in Fig. 2–9.

2.4. Synthetic surface generation

One way to calculate fractal dimension of a fractal geometry is using Power Spectral Density (PSD) method. PSD is a function which is earned by Fourier–transforming a signal’ s autocorrelation (Fig. 2–10). In the case of self–affine fractals, log–log plot of PSD function has the slope related to Hurst exponent as below (Lee et al., 1990; Babadagli and Develi, 2001; Jacobs et al., 2017):

$$(\text{SLOPE}) = \begin{cases} -2H - 1 & (\text{for curves}) \\ -2H - 2 & (\text{for surfaces}) \end{cases} \quad (2-18)$$

Using Eq. (2-12), we can assign the fractal dimension of self-affine fractals. In this thesis, training dataset for an Artificial Neural Network (ANN) is generated using an algorithm which is from Kanafi (2022).

This algorithm is a Matlab code that generates random fractal surfaces in the form of point cloud. There are five input parameters, which are Hurst exponent (H), amplitude standard deviation of surface amplitudes (σ), length of the resultant surface in x-axis direction (L_x), number of points in x-axis direction (m) and number of points in y-axis direction (n). With the input parameters, it first makes discrete isotropic PSD function on wavevector domain. By assigning a random phase on each wavevector and applying inverse fast Fourier transformation on the scaled root-mean-square of wavevectors, a point cloud of random fractal surface is generated on Cartesian coordinates domain. The generated point cloud is a rough

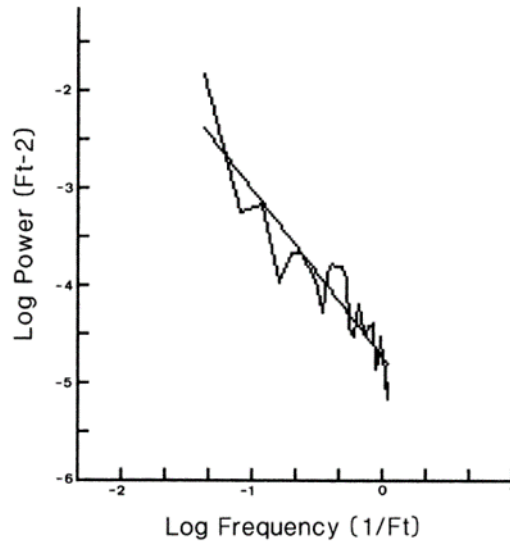


Figure 2-10. PSD of a joint profile (Carr and Warriner, 1989).

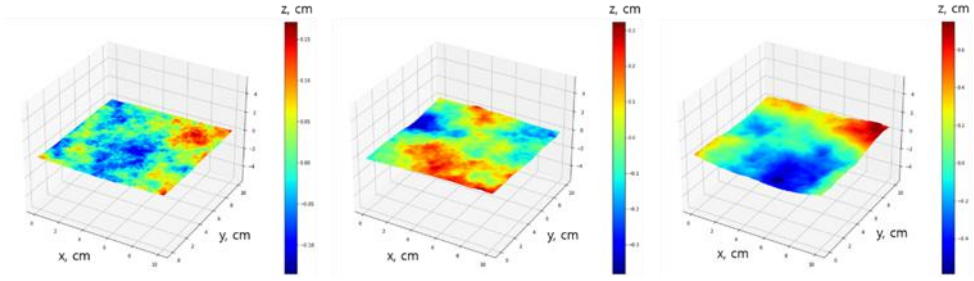


Figure 2–11. Synthetic rough surfaces generated by the algorithm. All three surfaces have the same JRC of 10 but different H . From the left, H is equal to 0.5, 0.7 and 0.9, respectively.

surface having m by n points with regular intervals in x - and y -axes directions and the standard deviation of heights, σ . In short, this is the inverse process of obtaining fractal dimension of fractal geometries using PSD method.

To make a training dataset, random rough surfaces were generated with different input parameters. As mentioned in section 2.2, previous scholars noted that H of most rock surfaces lies between 0.5 and 1.0, thus the input H was picked to be a random number between 0.5 and 1.0. Also, the σ was randomly picked to make JRC of the resultant surfaces to be in the range between 0 and 20 considering the pre-determined H value. Since the reference profiles in Fig. 2–1 are 10 cm long, L_x , m and n were fixed as 10 cm, 1,000 and 1,000, respectively. In Fig. 2–11, it is shown that the micro-scale roughness develops more as H gets smaller as mentioned in section 2.2.

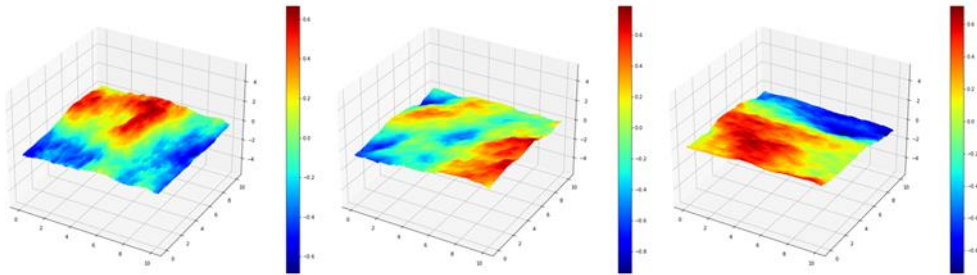


Figure 2–12. Generated surfaces with roughness anisotropy.

Also, to imitate actual rock surfaces having roughness anisotropy, PSD function was scaled at different rates depending on the direction. More isotropic surfaces were prone to be generated so that the JRC difference between two orthogonal directions does not exceed 10. Fig. 2-12 shows the most anisotropic surfaces among the generated surfaces.

2.5. Calculating JRC of the generated surfaces

To use the synthetic point clouds generated in section 2.4, they should be labeled with their JRC values. Since the point clouds have $1,000 \times 1,000$ points placed with equal interval on $10 \times 10 \text{ cm}^2$ area, thousand roughness profiles of 10 cm length having 0.1 cm sampling interval can be obtained for x-axis direction. After obtaining their Z_2 and JRC using Eq. (2-8) and (2-17), thousand JRC values in x-axis direction were averaged into one representative JRC value; JRC_x . Detailed process is explained below.

An artificial Barton comb was employed to get the roughness profiles from the generated surfaces. When we obtain a profile using a Barton comb, the height of a pin is determined to be the height of the highest rough feature among the asperities inside the pin as illustrated in Fig. 2-9. Therefore, each of the roughness profiles obtained from the generated surface was divided by the pin diameter, 0.8 mm (pin diameter of the author's comb), and each interval was set to have the constant height which is the maximum height in it (Fig. 2-13). As mentioned in Tatone and Grasselli (2010), it is better to choose sampling interval, Δx , larger than a pin diameter of the comb. Thus, Δx was set to be 1 mm in Eq. (2-8) and the last equation in Eq. (2-17) was used to calculate JRC of each profile obtained by the artificial comb. After calculating JRC of the 1,000 profiles in x-axis direction, the JRC values were averaged into one JRC (JRC_x) to label the

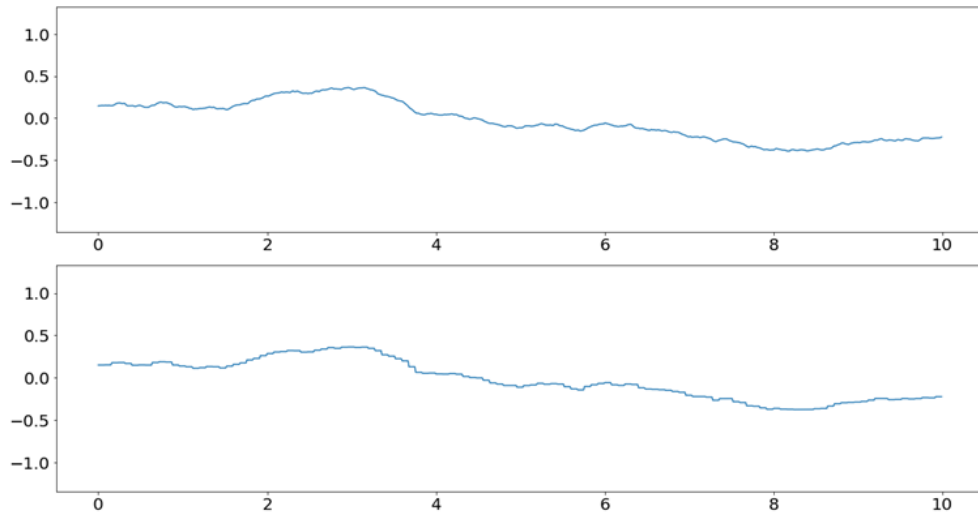


Figure 2–13. Rough profile from a generated surface (top) and the same profile after applying Barton comb (bottom). Digits in axes are in cm unit.

corresponding surface. The JRC-labeled point clouds are post-processed in the upcoming chapter to be the training dataset for an ANN.

Chapter 3. TLS precision

3D laser scanning is employed in many different fields such as construction, manufacturing, autonomous driving and forensic since it can duplicate things in real world in the form of 3D point cloud quickly. Since it is being more and more popular in rock mechanics and rock engineering, a survey on the laser scanning has been written as an additional article in the ISRM orange book (Feng and Röshoff, 2015). According to the article, laser scanning can be used for site characterization of a rock exposure, quality control of tunnel blasting, deformation monitoring, improvement of input data for numerical modeling and many other purposes.

In this chapter, basics of TLS and the reasons why it is important to know about the precision are explained first. In addition, algorithms to simulate noises in TLS data are introduced and applied on the synthetic rough surfaces generated in the previous chapter.

3.1. Basics of TLS

TLS is usually installed on the ground with a tripod, which looks like Fig. 3–1 (a). As shown in Fig. 3–1 (b), laser beam emitted from the laser diode is reflected through a mirror and extends outward. TLS uses a rotating mirror to scan all the surrounding area in a short time since it is difficult to rotate the laser diode due to its weight. Laser stretches out after being reflected by the mirror while the mirror and the whole device rotate 360 degrees in vertical and horizontal direction, respectively. Once the mirror turns 360 degrees in vertical direction, the device rotates horizontally with a small

(a)



(b)

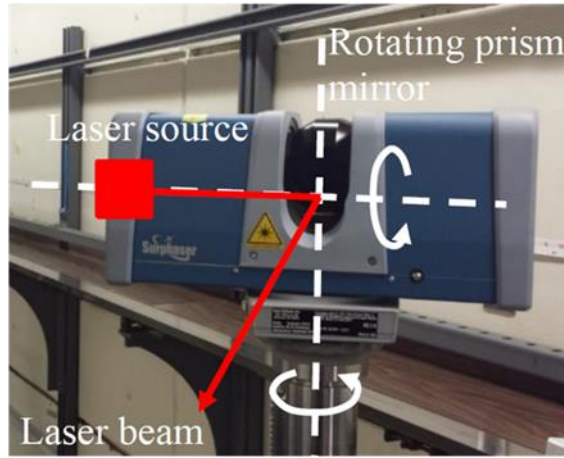


Figure 3–1. (a) TLS outlook (Faro Focus S 350+) and (b) rotating direction (horizontal/vertical) of the laser beam (Muralikrishnan, 2021).

angle interval. After the emitted laser reaches a surface, it is reflected and some of the scattered light comes back to the device to be detected. There is a unit named rangefinder inside the TLS, which calculates the travel distance of the laser by catching the difference between the emitted and returned light. By emitting the laser discretely, TLS can scan the surrounding area and save it as a point cloud quickly.

The stored data consist of the Cartesian coordinate and intensity of each recorded point. Also, each point has color information when the RGB color mode is set before scanning. In conjunction with the rangefinder, angle encoder is a sensor inside TLS, which records the vertical and horizontal angle of the laser; Φ and θ in Fig. 3–2. In this way, point clouds are firstly recorded in polar coordinates and then converted into the Cartesian coordinates through a linear transformation. The intensity of each detected laser is also measured and recorded in the data. Yet, the stored value of intensity is not a raw datum, being often scaled by the manufacturers in unknown ways (Schmitz et al., 2019).

Commercial TLS devices are usually divided into two types: 1) Time-of-

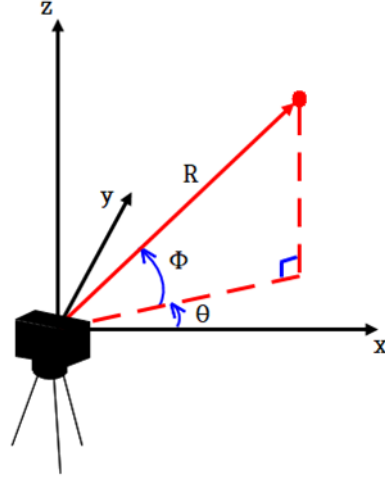


Figure 3–2. Polar coordinates of a detected target point. R , Φ and θ denote the range, vertical angle and horizontal angle, respectively.

Flight (TOF) type and 2) Amplitude–Modulated Continuous Wave (AMCW) ranging (=Phase–shift) type. Generally, the TOF type TLS can run at a distance farther than the AMCW type scanners (e.g. a few km) while AMCW type scanners can scan more precisely than the TOF type scanners. Here is the brief explanation on both types of the laser scanner:

- 1) TOF: Rangefinder in TOF type scanner measures the time difference between emitted and returned laser. Distance between the device and target is calculated by the equation below:

$$R = \frac{ct}{2} \quad (3-1)$$

where R , c and t represent range, speed and travel time of the light, respectively.

- 2) AMCW: AMCW type scanners emit amplitude–modulated waves and the rangefinder calculates the range by using the measured value of the

phase difference between the emitted and returned laser, φ , caused by the round trip. The equation is,

$$R = \frac{\lambda}{4\pi} \varphi \quad (0 \leq \varphi < 2\pi) \quad (3-2)$$

where λ is wavelength of the amplitude-modulated wave. In this equation, if R exceeds the half of λ , the phase difference is more than 2π so that the detector will judge the phase-shift to be $\varphi - 2n\pi$, where n is an unknown natural number. Therefore, for the AMCW scanner to run at long distances, wavelength of the modulated wave should be set large. However, if noise occurs in φ term in Eq. (3-2), it will be amplified more as λ gets larger, leading precision of the rangefinder to get worse. Accordingly, most AMCW type scanners employ two or three waves having different wavelengths. They use the shorter wave to measure precise phase-shift, using the longer one to calculate the unknown value, n . In this way, they can carry out scanning at considerably long distance with high precision (e.g. hundreds of meters).

In this thesis, two AMCW type TLS devices, Faro Focus S 350+ and Faro Focus S 350 are employed. Their technical specification is shown in Table 3-1. The only difference between the devices is the magnitude of range noise and Faro Focus S 350+ is more precise.

Table 3–1. Technical specifications of Faro Focus S 350 + and S 350 (Faro, 2021)

Faro Focus S 350+		Faro Focus S 350
Measurable Range	90% Reflectivity	10% Reflectivity
	0.6 ~ 350 m	0.6 ~ 150 m
		2% Reflectivity
		0.6 ~ 50 m
Step Size	0.009° (for both vertical and horizontal angle)	
Max. Scan Speed	97 Hz (for vertical angle)	
Beam Diameter at exit	2.12 mm (1/e)	
Beam Divergence	0.3 mrad (1/e)	
Range Noise	@ 10 m Range	
	90% Reflectivity	10% Reflectivity
	0.1 mm	0.3 mm
	2% Reflectivity	10% Reflectivity
Range Noise	@ 25 m Range	
	90% Reflectivity	10% Reflectivity
	0.2 mm	0.5 mm
	2% Reflectivity	10% Reflectivity
		1.6 mm
		0.3 mm
		0.5 mm
		2.0 mm
Angular Accuracy	19 arcsec (for both vertical and horizontal angle)	

3.2. Factors disturbing TLS precision

Fig. 3–3 schematically shows the meaning of the terms, accuracy and precision. Accuracy is a measure representing how close the measurements are to the actual value while precision means how close the measurements are to each other (Soudarissanane., 2016). Generally, systematic errors determine the accuracy of a device while random errors determine the precision. Here, systematic error denotes the consistent error induced by miscalibration (e.g. inclination of rotation axis), which can be fixed by calibration. Random error, on the other hand, is unpredictable and not a subject of calibration, which occurs in the form of Gaussian distribution.

Since the target of interest of this thesis is a small area of joint surfaces having micro–scale rough features, precision is a matter of importance. On the other hand, accuracy is less important because point cloud of such joint surfaces is arranged in a later section. Therefore, noise sources that disturb TLS precision are covered in detail while factors relevant to accuracy are

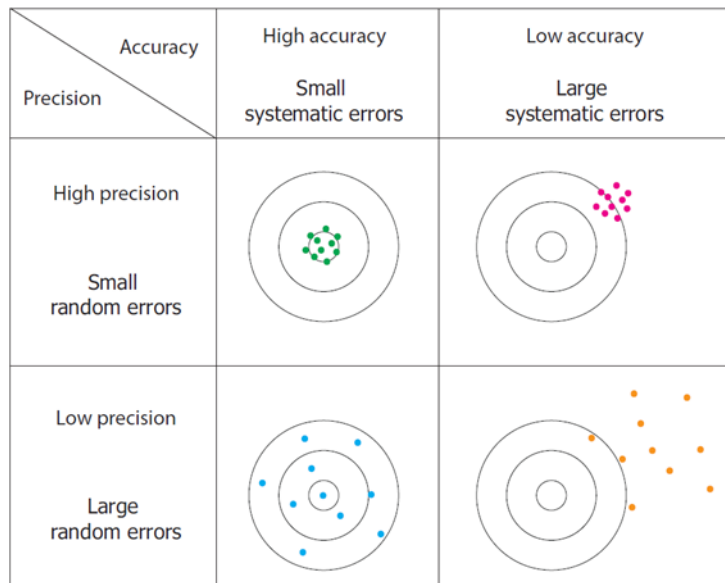


Figure 3–3. Difference between accuracy and precision (Soudarissanane, 2016).

not dealt with (Refer to Muralikrishnan, 2021 for knowledge about TLS accuracy). In this chapter, factors affecting TLS precision are classified into three; 1) range noise, 2) angular noise and 3) mixed-pixel effect.

3.3. Measuring roughness of joint using TLS

Previously, several attempts have been made to measure roughness of rock discontinuities using TLS. Although their purpose was not always to calculate JRC, those studies are briefly looked over in this section.

Fardin et al. (2004) used an old TLS model, LARA of Z+F, to scan a rock exposure from 10 m distance and obtain its point cloud for roughness characterization. The authors tried to quantify roughness with two parameters, fractal dimension and amplitude parameter, measured from the point cloud using a method called Roughness–Length method (RL method). To observe the scale effect of roughness, those parameters were calculated while changing the size of sampling window. As a result, it was confirmed that the roughness value converges as the window size increases and it is possible to calculate the primary roughness (large-scale roughness) using the TLS. However, the authors stated that it is difficult to calculate the secondary roughness (small-scale roughness) using the TLS due to resolution and noise of the data.

Kemeny and Turner (2008) presented two different methods for estimating roughness using triangulated mesh of joint surfaces constructed from TLS scan data. One is to project the orientation of each triangle of the joint onto the stereonet. By observing the degree of scattering from the mean orientation of the surface, they could get information about the dilatation angle of the joint as shown in Fig. 3–4. The other method is to calculate JRC

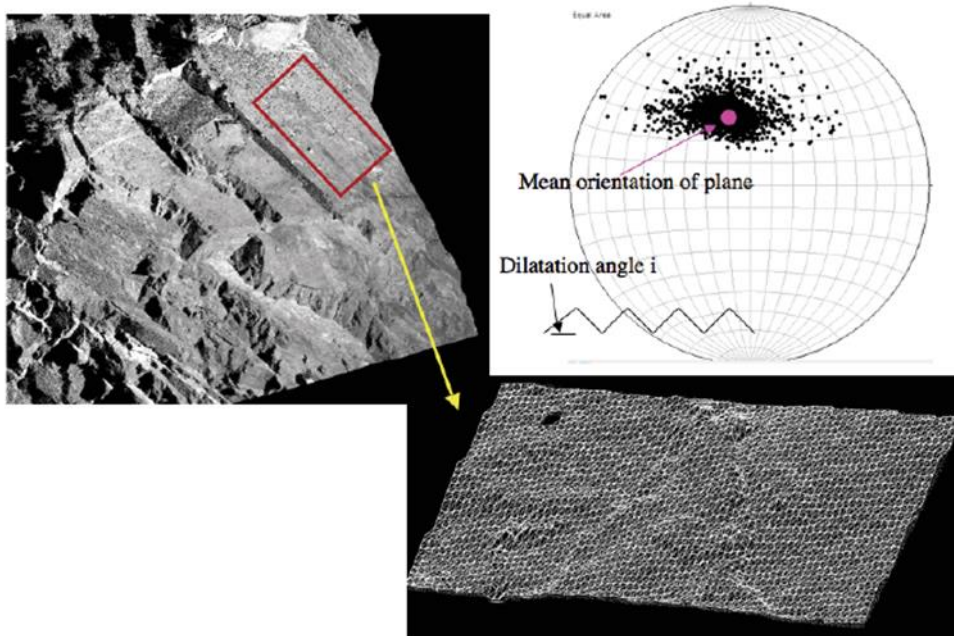


Figure 3–4. Schematic images showing the process of roughness estimation by stereonet projection (Kemeny and Turner, 2008).

of the roughness profiles obtained from the mesh data. Roughness profiles were extracted by cross-sectioning the mesh in the potential shear direction and their Z_2 and JRC were calculated by using Eq. (2–8) and (2–9). In this report, the authors said that if the size of triangular mesh is smaller than the error level of the scanner, the error would affect the roughness measurement.

Gigli and Casagli (2011) measured roughness of rock joint from TLS scan data using searching cubes with different dimension (0.1, 0.2, 0.4, 1, 2 m). As the cube moves across the point cloud of the joint, best-fit plane of points inside the cube was plotted on stereonet. Same with Kemeny and Turner (2008), they tried to quantify roughness by observing the degree of scattering from the mean orientation of the joint. They warned that the validity of this method depends on the accuracy of the device and in particular, measurements can be overestimated due to the noise when measuring roughness at a small scale.

Marsch et al. (2020) compared the applicability of four different 3D scanners including TLS (Faro Focus 3D X 330 HDR) in roughness estimation for rock surfaces. After scanning rock specimens with various roughness using each device, they measured the error level and JRC of point clouds of the specimens. Here, JRC was obtained by extracting roughness profiles from the triangulated mesh obtained from the point cloud. As a result, TLS scan data was revealed to have the highest error level and the most inaccurate JRC. Accordingly, the authors said that it is better to avoid measuring small-scale roughness using the TLS.

Bitenc et al. (2019) scanned rock joint samples using a TLS, Riegl VZ400, under various scanning configurations. The authors employed wavelet decomposition techniques to separate noise from the scan data. Performance of the techniques was evaluated by measuring Grasselli parameter of the noise-separated data and comparing it with the reference value. As a result, it was confirmed that roughness can be measured more accurately through wavelet decomposition. However, there is a process to select a threshold value needed for the decomposition and the threshold selection method should be chosen based on roughness of the target surface.

According to the previous works introduced above, it is difficult to measure roughness in small-scale due to the existence of noise in TLS scan data. In this thesis, noise simulation and an ANN are employed to deal with the noise.

3.4. Range and angular noise

When laser beam is reflected from a planar Lambertian reflector (Fig. 3–7) and reaches to a detector in TLS, power of received laser is calculated as

below (Soudarissanane et al., 2011):

$$P_{\text{received}} = P_{\text{emitted}} \frac{\cos \alpha}{\rho^2} \pi \gamma \eta_{\text{sys}} \eta_{\text{atm}} \quad (3-3)$$

where P_{received} , P_{emitted} , α , ρ , γ , η_{sys} and η_{atm} denote received power, emitted power, incidence angle between the beam and normal of the reflector, range, surface reflectivity, systematic power loss and atmospheric power loss, respectively. This amount of received power determines the Signal-to-Noise Ratio (SNR) in range measurement. Accordingly, random noise is added to the measured value of the range in the direction of the laser beam, which is called range noise.

Being independent to the range noise, another type of random noise existing in the angle encoder is called angular noise. In other words, noise in Φ and θ in Fig. 3-2 is the angular noise.

When we repeat TLS scanning, position of scanned points changes slightly every time even if the scanning is performed right at the same location. Therefore, it is difficult to measure point-wise noise level so that many researchers have tried to estimate the noise level by scanning planar objects and calculating mean distance between their point cloud and the best-fit plane. Furthermore, it is also very hard to decompose the measured noise into range and angular noise present in point clouds since they are mixed. Given this situation, authors of the following articles tried characterizing those TLS noises.

Soudarissanane et al. (2011) assumed that the level of range noise is determined by Eq. (3-3), and measured the range noise acting on planar

surfaces in different range and incidence angle. In this way, they could validate the effect of range and incidence angle on range noise level and by conducting indoor TLS scanning, they found a better position for locating TLS that minimizes the noise level.

Wujanz et al. (2017) also stated that range noise level of TLS is influenced by the range, incidence angle and surface characteristics of target. In addition, they assumed that the raw intensity values of TLS scan data contain most of the information of those variables and range noise level can be estimated by using the intensity as the only parameter. They derived the empirical equation relating only the intensity to range noise level after carrying out some scanning and showed that all the data obtained from scanning with different settings always lie on that equation. In this article, 1D scanning mode or planar surfaces whose normal is semi-perpendicular to the laser beam were utilized to exclude the effect of angular noise.

Agreeing with Wujanz et al. (2017), Schmitz et al. (2019) said that range noise level of TLS is predictable by using only the intensity. However, they pointed out that most of TLS devices offer scaled value of intensity and their manufacturers do not open the scaling method to the public. After carrying out a lot of scanning, they revealed that the scaled intensity can also be used for predicting range noise level, but in limited circumstances. Additionally, they could calculate range and angular noise level from point cloud of inclined planar surfaces using variance component estimation.

In the above articles, factors influencing the noise level of TLS were figured out and intensity-based models predicting range noise level have been suggested. Yet, not much research has been carried out on angular noise and in many works, values specified in the device brochures are generally used for estimating the angular noise level (Holst et al., 2014; Wujanz et al.,

2017).

3.5. Mixed-pixel effect

Laser emitted from a TLS diverges as it passes through the atmosphere as shown in Fig. 3-5(a). Therefore, diameter of beam cross-section gets larger as it moves farther and it can be a few to several tens of millimeters depending on the range. It makes laser beam to meet with the target in an area rather than a dot. Hence, the range value that rangefinder records becomes a spatially averaged value for the beam contact area. This phenomenon is called mixed-pixel effect.

Mixed-pixel effect occurs mainly near the edge of a surface since the effect becomes severe when there is rapid range difference inside the beam width, and is thus also called the edge effect. Fig. 3-5-(c) shows an illustration of resultant points (i.e. mixed-pixels) which do not exist in reality but appear when the laser beam falls on the edge of a surface as shown in Fig. 3-5(b).

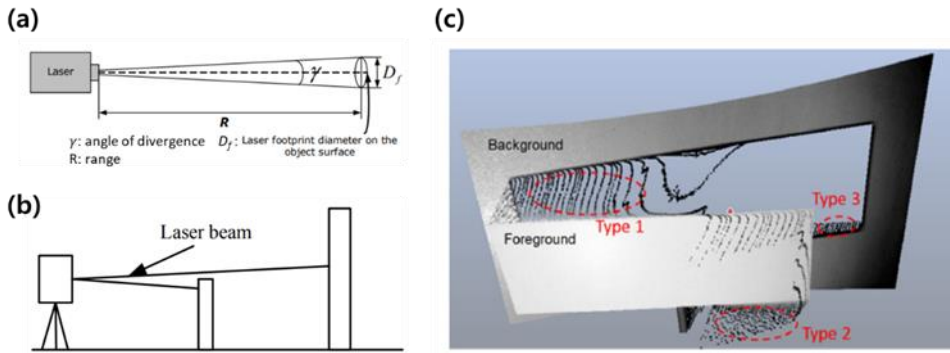


Figure 3-5. (a): Divergence of laser beam. (b): Laser beam falling on a surface edge. (c): Mixed-pixels in a point cloud. Different types of mixed-pixels can be made depending on the range difference between foreground and background (a, b: Reshetyuk, 2009, c: Wang et al., 2016).

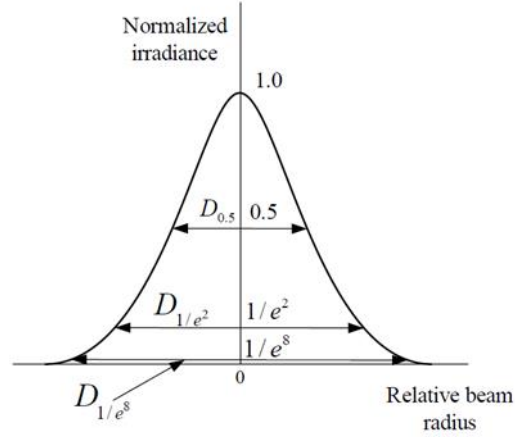


Figure 3–6. Irradiance distribution in the cross–section of a Gaussian beam (Reshetuk, 2009).

In this section, principles of the mixed–pixel effect appearing in AMCW type scanners are explained referring to Wang et al. (2016) and Chaudhry et al. (2019). Since TLS devices used in this thesis are AMCW type, mixed–pixel effect in TOF or other types of TLS will not be addressed.

In general, after a laser beam is emitted, the width decreases until it reaches a position called the beam waist, where it has the smallest diameter. When the beam moves further from this position, its radius expands and is calculated as below:

$$w(R) = w_0 \sqrt{1 + \left(\frac{\lambda R}{\pi w_0^2} \right)^2} \quad (3-4)$$

where w , w_0 , R and λ denote beam radius, radius of beam waist, range and wavelength of the laser.

Beam diameter of a laser beam is generally defined based on the irradiance distribution in the cross–section of a Gaussian beam. As shown in Fig. 3–

6, Gaussian beam represents that the cross-sectional irradiance of the beam is distributed in the form of a Gaussian distribution. In the figure, the beam diameter is defined in various ways. For example, beam diameter based on $1/e^2$ irradiance (D_{1/e^2}) means the distance between the opposite points where the irradiance is $1/e^2$ times the irradiance at the beam center (Marshall and Stutz, 2012). Provided that the beam radius based on $1/e^2$ irradiance is w , the irradiance at an arbitrary point inside the beam, i , is calculated as below:

$$E_i = E_0 \exp\left(-\frac{2\rho_i^2}{w_i^2}\right) \quad (3-5)$$

where E_0 is the irradiance at the beam center, and ρ_i is the distance between i and the beam center. Eq. (3-6) is used instead of Eq. (3-5) when the beam radius is based on $1/e$ irradiance.

$$E_i = E_0 \exp\left(-\frac{\rho_i^2}{w_i^2}\right) \quad (3-6)$$

For the surface into which a beam enters, let a small area element inside the beam width be i and assume its irradiance to be E_i in Eq. (3-5). Since irradiance means the power of incident light over unit area, the power of the incident laser on i can be calculated by the following equation:

$$P_{o,i} = E_i A_i \cos \alpha_i \quad (3-7)$$

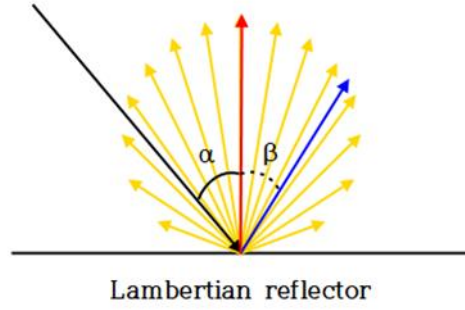


Figure 3–7. Light reflected from a Lambertian reflector has the same radiance regardless of the angle from the normal. Yellow arrows represent the intensity magnitude of the reflected light while red and blue arrows represent the surface normal and an arbitrary direction, respectively (After Photonik and Sandner, 2015).

where A_i is the area of i , and α_i is the incidence angle between laser beam and the normal direction of i . Total power of the light reflected from i is calculated by multiplying the incident power, $P_{o,i}$, and the reflectance of i , R_i ($0 \sim 1$), as below:

$$P_{r,i} = P_{o,i} R_i \quad (3-8)$$

If i is assumed to be the Lambertian reflector, the intensity of scattered laser is calculated as following equation:

$$I = I_0 \cos \beta \quad (3-9)$$

In this equation, β represents the angle between the normal of the reflector and an arbitrary direction as shown in Fig. 3–7. Also, I_0 is the intensity where β equals zero. Since intensity represents power per solid angle,

total power of the reflected light, P , can be calculated as below:

$$\begin{aligned}
 P &= \int_0^{2\pi} I \, d\omega = \int_0^{2\pi} I_0 \cos \beta \, d\omega \\
 &= \int_0^{\frac{\pi}{2}} \int_0^{2\pi} I_0 \sin \beta \cos \beta \, d\theta \, d\beta = \pi I_0 \\
 &\rightarrow I = \frac{P}{\pi} \cos \beta
 \end{aligned} \tag{3-10}$$

Here, ω and θ denote the solid angle and the azimuthal angle about the surface normal, respectively. In the case of TLS, laser source and detector are at the same position ($\beta = \alpha_i$). Therefore, the intensity of the reflected light toward the detector follows:

$$I_{r,i} = \frac{P_{r,i}}{\pi} \cos \alpha_i \tag{3-11}$$

Also, the amount of power detected at the detector, $P_{d,i}$, is calculated by multiplying intensity and corresponding solid angle as following equation:

$$P_{d,i} = I_{r,i} \frac{A_d}{d_i^2} \tag{3-12}$$

where A_d and d_i denote the area of the detector and distance between i and the detector, respectively. In the meanwhile, we can assume that the power of the laser being emitted, P_e , is a cosine function of time as below:

$$P_e = P_0 \cos\left(\frac{2\pi c}{\lambda} t\right) \quad (3-13)$$

where P_0 is the amplitude, c is the speed of light, λ is the modulation wavelength, and t is time after the emission. Thus, total power of detected laser reflected from i can be expressed by a function of time as below:

$$P_i = P_{d,i} \cos\left(\frac{2\pi c}{\lambda} t + \varphi_i\right) \quad (3-14)$$

where $\varphi_i = \frac{4\pi}{\lambda} d_i$

where φ_i represents the phase-shift of the modulated wave. Therefore, the total amount of detected power can be calculated by summing up the detected power from all the area element as following equation:

$$P = P_d \cos\left(\frac{2\pi c}{\lambda} t + \varphi\right) = \sum_i P_{d,i} \cos\left(\frac{2\pi c}{\lambda} t + \varphi_i\right)$$

$$\rightarrow \begin{cases} P_d \cos \varphi = \sum_i P_{d,i} \cos \varphi_i \\ P_d \sin \varphi = \sum_i P_{d,i} \sin \varphi_i \end{cases} \quad (3-15)$$

where P_d and φ denote the amplitude of the function and the phase-shift, respectively. Given the equation, the phase-shift can be calculated as below:

$$\varphi = \arctan \left(\frac{\sum_i P_{d,i} \sin \varphi_i}{\sum_i P_{d,i} \cos \varphi_i} \right) \quad (3-16)$$

Finally, the range between the target and TLS is calculated by following equation.

$$d = \frac{\lambda}{4\pi} \varphi + \frac{\lambda}{2} N \quad (3-17)$$

where N denotes the unknown number of full cycles of the modulated wave. As mentioned in section 3.1, TLS employing more than two different modulation wavelengths uses shorter modulation wave to calculate the range precisely. Thus, λ in Eq. (3-17) denotes the shortest modulation wavelength and N can be calculated by using a larger modulation wavelength.

3.6. Synthetic noise application

In this section, TLS errors explained throughout section 3.4 and 3.5 are simulated on the surfaces generated in section 2.4. After the mixed-pixel effect is simulated first, range and angular noise are also applied on the surfaces sequentially.

Before simulating errors, the range of distance and incidence angle of interest have been restricted as below:

- ① Distance (= range): Based on section 3.4 and 3.5, error level increases as the distance between TLS and target increases. Therefore, if the

distance is too long, noise level becomes too large leading the roughness characterization unavailable. Furthermore, density of point cloud would be too sparse. In contrast, if the distance is too short, the purpose of measuring JRC in distance would not be achieved. In addition, if the range of noise level is too wide, it would be difficult for an ANN to learn about the TLS noises. Considering the above problems, the distance between TLS and joint surfaces is restricted to 8 ~ 12 m.

- ② Incidence angle: Incidence angle of laser determines density of point cloud. If density of point cloud is too sparse, it would be impossible to characterize roughness. In this thesis, 2,048 points in 100 cm² is required to utilize an ANN. Provided that step size of Faro Focus S 350+ and 350 is 0.009° for both vertical and horizontal directions according to Table 3-1, incidence angle has to be smaller than 43° at the maximum distance of interest, 12 m. Therefore, the range of incidence angle is restricted to 0 ~ 45° .

1) Mixed-pixel effect

Referring to Table 3-1, both TLSs have beam diameter of 2.12 mm at exit and full-angle divergence of 0.3 mrad. Here, these two values are based on 1/e irradiance. Accordingly, beam diameter, D , with respect to the range, R (m), will follow the below equation:

$$D = 2.12 + 2 \cdot 10^3 R \tan\left(\frac{0.3 \cdot 10^{-3}}{2}\right), \text{ mm} \quad (3-18)$$

Here, R is set as a random number between 8 and 12. Let O be one of a

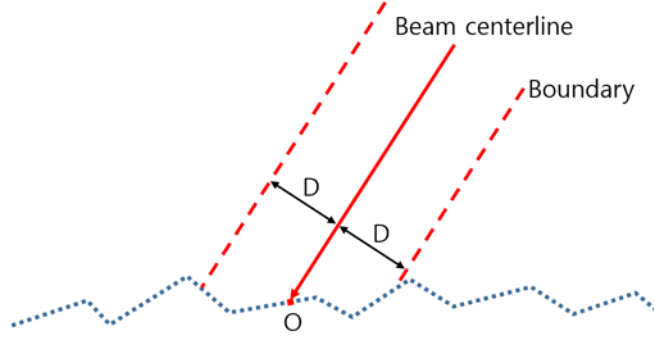


Figure 3-8. Determining the influencing area by setting the boundary.

million points that make up each surface generated in section 2.4. Incident direction of laser beam is denoted by a unit vector, \hat{b} , and O is set to be the intersecting point of the centerline of the beam and the surface as shown in Fig. 3-8. In addition, it is assumed that the incident directions of the points located inside the same beam are parallel to each other and a boundary is set to distinguish the points that affect the degree of mixed-pixel effect. Since the beam diameter is based on $1/e$ ($\sim 36\%$) of the maximum irradiance, the distance between the centerline and the boundary is set to D instead of $D/2$ to contain most of the laser.

Points inside the boundary is a set of n points, $P = \{p_1, p_2, \dots, p_i, \dots, p_n\}$, and $P_{d,i}$ in Eq. (3-12) can be expressed in terms of E_i by using Eq. (3-7), Eq. (3-8), and Eq. (3-11) as follow:

$$P_{d,i} = \frac{A_d}{d_i^2} \times \frac{\cos \alpha_i}{\pi} \times R_i \times E_i A_i \cos \alpha_i \quad (3-19)$$

When we approximate p_i to i in the equation, all the parameters having i as subscript become the corresponding values of p_i . Then, assume that all is

have the same R_i and d_i^2 since they are on the same surface and differences between d_i is so small compared to the distance between the surface and the device. By substituting the invariant part of Eq. (3-19) by k , following equation is obtained:

$$P_{d,i} = kE_i A_i \cos^2 \alpha_i \quad (3-20)$$

When all the elements (i) are projected on the xy-plane, they have the same x and y intervals. Therefore, it can be assumed that every i has the same projection area denoted by A_0 . Accordingly, the xy-plane projection of A_i is equal to A_0 and the following equation holds:

$$A_i = \frac{A_0}{|\hat{n}_i \cdot \hat{z}|} \quad (3-21)$$

In the equation, \hat{n}_i and \hat{z} represent the unit normal vector of A_i and the z unit vector in Cartesian coordinate system, respectively. By using \hat{b} and putting Eq. (3-21) in Eq. (3-20), following equation is obtained:

$$P_{d,i} = kE_i A_0 \frac{(\hat{b} \cdot \hat{n}_i)^2}{|\hat{n}_i \cdot \hat{z}|} \quad (3-22)$$

By putting this equation in Eq. (3-16), we can get:

$$\begin{aligned}
\varphi &= \arctan \left(\frac{\sum_i P_{d,i} \sin \varphi_i}{\sum_i P_{d,i} \cos \varphi_i} \right) \\
&= \arctan \left(\frac{\sum_i E_i \frac{(\hat{b} \cdot \hat{n}_i)^2}{|\hat{n}_i \cdot \hat{z}|} \sin \varphi_i}{\sum_i E_i \frac{(\hat{b} \cdot \hat{n}_i)^2}{|\hat{n}_i \cdot \hat{z}|} \cos \varphi_i} \right)
\end{aligned} \tag{3-23}$$

By expressing phase-shift at O as φ_0 , φ_i and φ can be represented as below:

$$\begin{aligned}
\varphi_i &= \varphi_0 + \Delta \varphi_i \\
\varphi &= \varphi_0 + \Delta \varphi
\end{aligned} \tag{3-24}$$

In this way, Eq. (3-23) can arranged as following equation:

$$\Delta \varphi = \arctan \left(\frac{\sum_i E_i \frac{(\hat{b} \cdot \hat{n}_i)^2}{|\hat{n}_i \cdot \hat{z}|} \sin \Delta \varphi_i}{\sum_i E_i \frac{(\hat{b} \cdot \hat{n}_i)^2}{|\hat{n}_i \cdot \hat{z}|} \cos \Delta \varphi_i} \right) \tag{3-25}$$

Referring to Eq. (3-17), relationship between $\Delta \varphi$ and Δd can be inferred as:

$$\Delta \varphi = \frac{4 \pi}{\lambda} \Delta d \quad (3-26)$$

Following equation is obtained as we arrange Eq. (3-25) in terms of Δd :

$$\Delta d = \frac{\lambda}{4 \pi} \arctan \left(\frac{\sum_i E_i \frac{(\hat{b} \cdot \hat{n}_i)^2}{|\hat{n}_i \cdot \hat{z}|} \sin \left(\frac{4 \pi}{\lambda} \Delta d_i \right)}{\sum_i E_i \frac{(\hat{b} \cdot \hat{n}_i)^2}{|\hat{n}_i \cdot \hat{z}|} \cos \left(\frac{4 \pi}{\lambda} \Delta d_i \right)} \right) \quad (3-27)$$

We can calculate the range after mixed-pixel effect has been applied by adding Δd to distance between TLS and O. In this equation, \hat{b} was set randomly to have the incidence angle less than 45 degrees and E_i can be obtained by using Eq. (3-6). Thus, \hat{n}_i and λ are all we need to know, which are the unit normal vector of i and the shortest modulation wavelength of Faro Focus S 350+ and 350. To get \hat{n}_i , vertex normal estimation, a

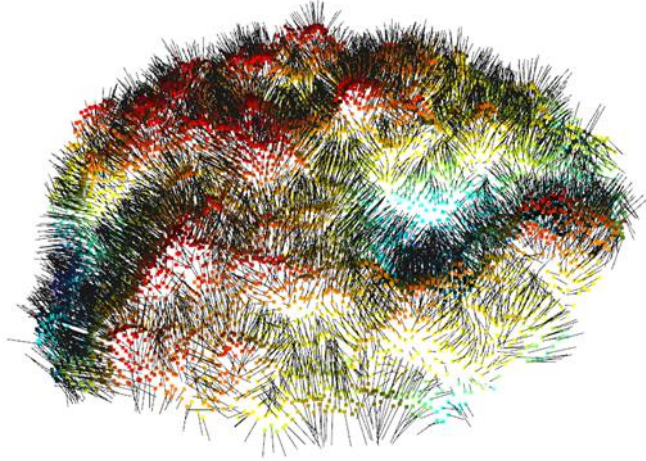


Figure 3–9. Normal vectors of all the points inside a beam area. Black thorns indicate the normal vectors.

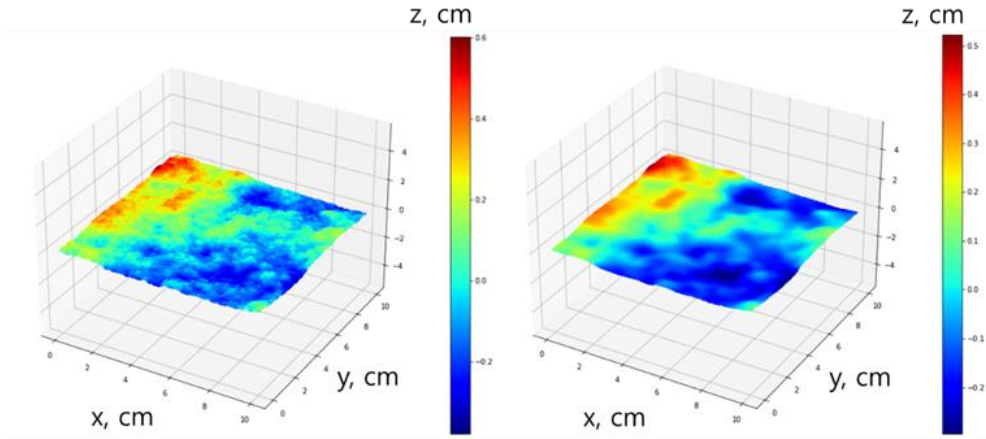


Figure 3–10. Point cloud of a rough surface whose JRC_x is 19.13 (left). And the same surface after adding the mixed–pixel effect (right). TLS 10 m away in z -axis direction was assumed in this case.

function from open3d library in python, was employed. This function calculates the normal vector of every point by using positional relationship with the adjacent points. Fig. 3–9 shows the normal vectors obtained by the function for points inside a beam boundary. On the other hand, the shortest modulation wavelength is not known to the public since it is a confidential information of the manufacturer. Yet, it has once been revealed that the former Faro TLS model had the shortest modulation wavelength of 2.4 m and there is an article stating that setting the shortest modulation wavelength around 1 m is reasonable (Chaudhry et al., 2021; Wang et al., 2016). When I tried applying the mixed–pixel effect on several synthetic rough surfaces, setting the wavelength as 2.4 m and 1 m did not show any differences in the resultant point clouds. Therefore, λ was set as 2.4 m in this thesis.

Through the above process, a code was written to simulate the mixed–pixel effect on the synthetic surfaces. Fig. 3–10 shows an example of resultant surfaces.

2) Range noise

On all the points where mixed-pixel effect was applied, noise in Gaussian distribution was added in the beam direction. Here, standard deviation of the distribution was assigned a random number between 0 and 0.4 mm referring to Table 3-1 and considering the target distance of 8 to 12 m.

3) Angular noise

Since the angular noise is the noise present in angle encoder, it is assumed that the angular noise is generated in the form of Gaussian distribution on Φ and θ in Fig. 3-2. For each surface where mixed-pixel effect was applied on, a plane orthogonal to the beam direction has been assumed. A random direction on that plane was set to be the horizontal direction, and its in-plane orthogonal direction was set to be the vertical direction. Then, Gaussian noise was added in each direction. Referring to angular accuracy in Table 3-1, the standard deviation for each noise was assigned as below:

$$\sigma_{\text{horizontal}} = \sigma_{\text{vertical}} = 0.09211 \times R \text{ (mm)} \quad (3-28)$$

where the unit of R is meter.

3.7. Training data generation

Following the steps introduced in section 3.6, synthetic surfaces on which TLS noises are applied were generated. Considering the step size in Table 3-1, 2 ~ 4,000 points are contained in 100 cm^2 area when it is scanned at

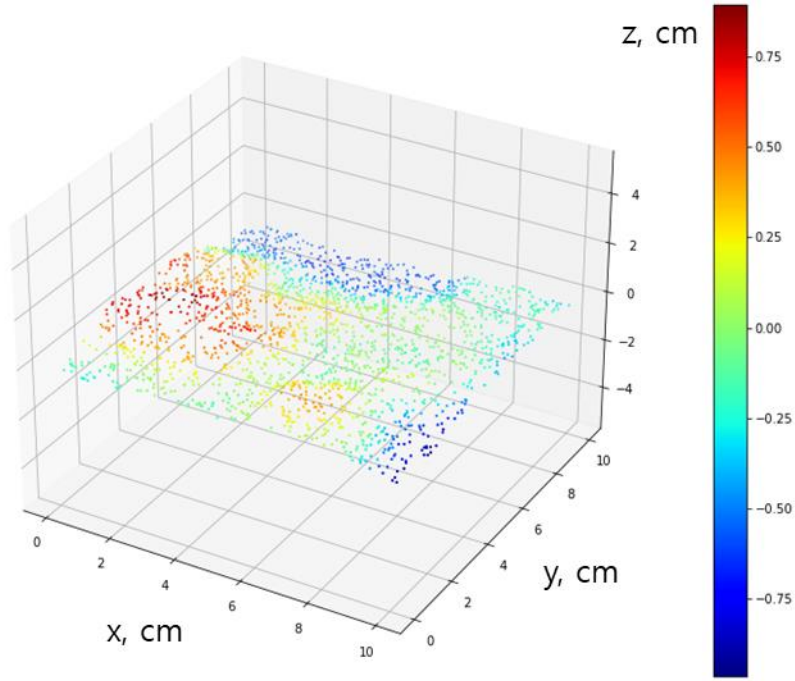


Figure 3–11. One of the training data. JRC_x of this surface is 18.98.

8 ~ 12 m distance. Thus, only 2,048 points were selected randomly from each synthetic surfaces to imitate surfaces scanned by TLS.

Finally, total 20,480 noise–applied surfaces having different JRC_x , degree of anisotropy, fractal dimension, beam direction and range have been created. Since each surface has JRC_y (JRC in y –axis direction) different from JRC_x , all the surfaces were reflected over $y=x$ and labeled with corresponding JRC_x (which is equal to JRC_y before reflection) in order to augment the amount of training data. In this way, total 40,960 synthetic surfaces were obtained and became the training dataset for an ANN. The whole data generation process can be summarized as follows:

- ① Generate point cloud of rough surfaces using the fractal–based algorithm.
- ② Label each surface with its JRC_x .
- ③ Apply TLS noises (Mixed–pixel effect, range noise and angular noise)

on the surfaces.

- ④ Pick 2,048 points from each surface.
- ⑤ Augment the data by reflecting the surfaces over $y=x$.

Fig. 3-11 shows one of the final product.

Chapter 4. ANN estimating JRC of TLS data

Artificial Neural Networks can solve problems that were thought to be solvable only by humans. Distinguishing facial expressions from human face photos is an example of such problems. To solve that problem with traditional algorithm is very challenging since the rules to be established are too complex and it might not work as the angle or position of the face is slightly changed. However, if an ANN is trained with a sufficient amount of the photos, it can even classify the unseen photos with high accuracy using its ability to generalize.

In this chapter, assuming that the ANN can learn how to distinguish the noise from the TLS scan data, an ANN called PointNet is trained with the synthetic training dataset generated at former chapters and validated with real data.

4.1. PointNet

Point cloud data means a set of points expressed in the form of Cartesian coordinates. Therefore, if a point cloud consists of N points, it can be represented by an $N \times 3$ matrix. Since laser and optical scanners are widely used for various purposes these days, methods to handle point cloud data are being studied a lot. Among such methods, an ANN called PointNet is employed in this thesis. PointNet, which has been developed by Qi et al. (2017), is a deep neural network that can directly consume raw point cloud and perform classification or segmentation.

Qi et al. (2017) focused on three characteristics of point cloud to handle it with an ANN; 1) Unorderliness, 2) interaction between points, and 3)

invariance under rigid or affine transformation. First, that a point cloud is unordered means its shape and properties are not affected by the order of the points constituting it (i.e. changing the order of rows in the $N \times 3$ matrix). Also, the second one represents that each point of a point cloud does not contain any information when viewed separately, and the meaning of a point cloud is determined according to the relationship between all the points. Finally, the third one means that the shape and type of a point cloud do not change when rigid or affine transformation (spatial translation and rotation) is applied on it. These characteristics make it challenging for the ANN to handle point cloud data.

ANNs prior to PointNet used to accept pre-processed data such as mesh, voxels and converted 2D images rather than the raw point cloud to handle the above problems. Given that situation, PointNet became a pioneering network that directly receives and processes raw point clouds. The strategies used by Qi et al. (2017) to solve the aforementioned problems are as follows. First, a symmetric function is utilized to aggregate the information of unordered points. Here, a symmetric function means a function that produces the same result regardless of the order of input values, such as addition and multiplication. PointNet gathers the features of each point of a point cloud by using max-pooling as the symmetric function.

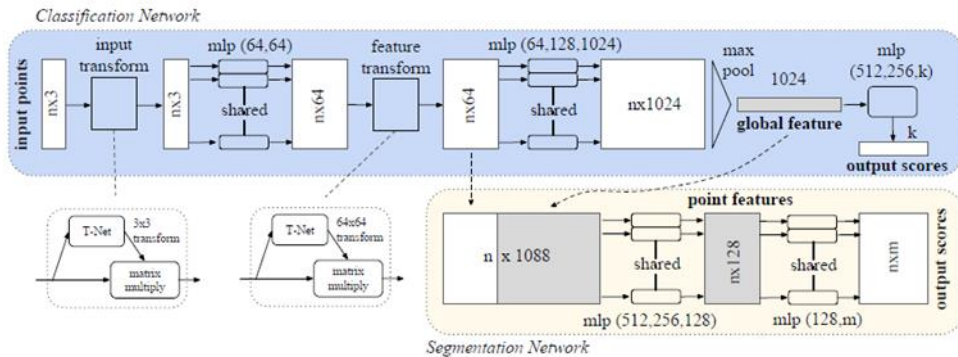


Figure 4–1. PointNet structure (Qi et al., 2017).

To solve the second problem, the local and the global characteristics of point clouds are combined together by merging the point-wise features and the max-pooled features. Finally, a module named T-net which is a transformation matrix consisting of trainable variables is utilized. Using the T-net, the same result could be achieved regardless of the spatial transformation of the point cloud after training the network with point clouds having different arrangement.

Fig. 4-1 shows the structure of PointNet. Dimension of the point-wise features is changed through multi-layer perceptron consisting of 1×3 and 1×1 convolutional layers, and the features of all points are aggregated by the max-pooling layer. After passing through the max-pooling layer, fully-connected layers are placed to conduct classification. In the article, PointNet has been evaluated with benchmark point cloud datasets. As a result, it was confirmed that PointNet had the state-of-the-art performance at that time.

4.2. Test data acquisition

To train and validate an ANN model, point clouds of real rock surfaces are required. Therefore, point clouds obtained from two different TLSs (Faro Focus S 350 and 350+) are used in this thesis. Field scanning was conducted on a rock exposure using Faro Focus S 350+, and data of the same target from Faro Focus S 350 was obtained from the author of Lee (2020).

The site of interest is a granite outcrop of Gwanak mountain in Seoul, Korea. Faro Focus S 350+ was installed about 11 m in front of the outcrop as shown in Fig. 4-2(b). Among the joint surfaces in the outcrop, 17 surfaces were selected and framed by white papers which had been cut to have square of



Figure 4–2. Picture of (a) granite rock exposure and target surfaces framed by white papers, and (b) scanning configuration.

$15 \times 15 \text{ cm}^2$ inside. Scanning area was restricted to barely include the rock exposure to reduce the scanning time, and thus it took about 15 minutes even though the highest precision and resolution mode was set.

Before the scanning, JRC of the 17 surfaces was measured by hand using a Barton comb. Pin diameter of the comb is 0.8 mm, and six profiles were acquired for each surface. Among the profiles, three are for one direction

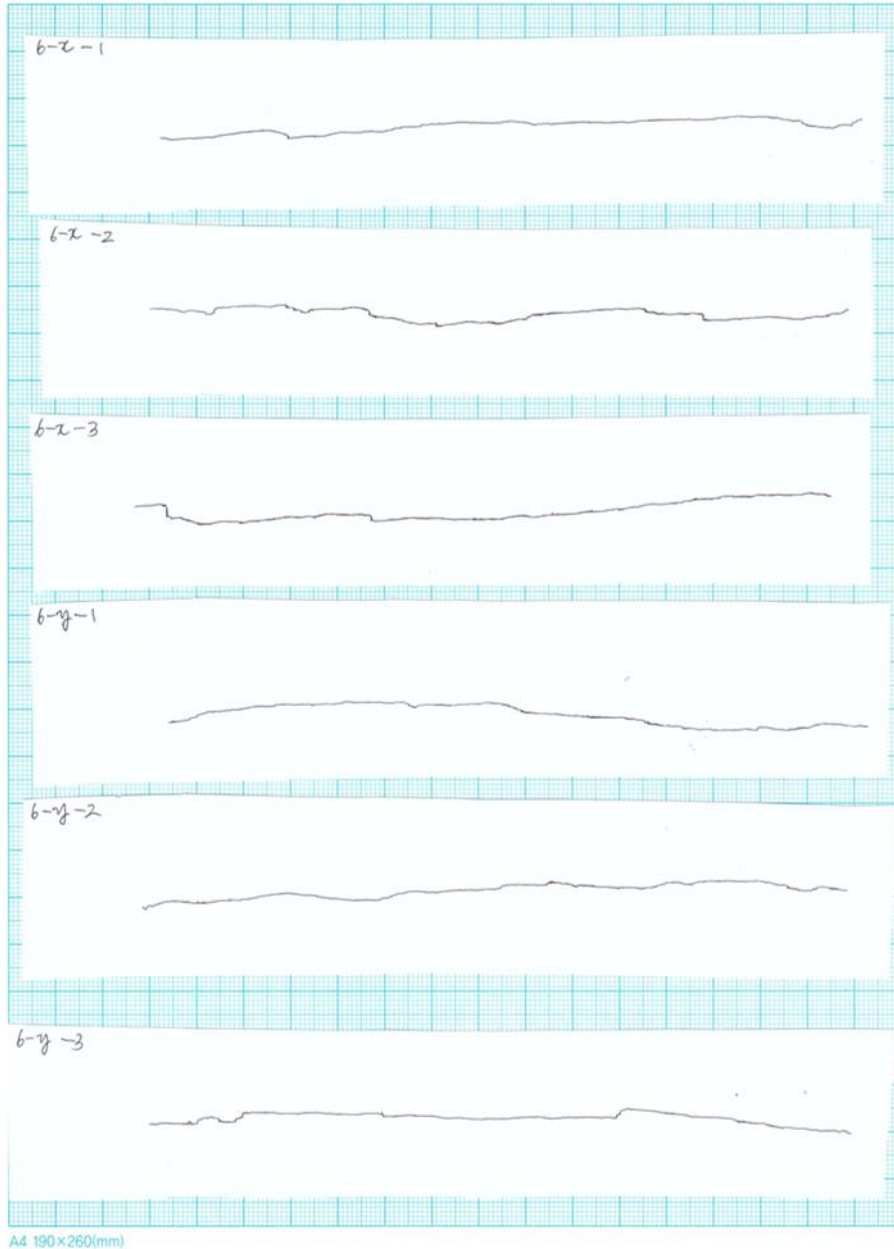


Figure 4-3. Six roughness profiles acquired from a surface. Index of the surfaces are shown in Appendix A, Fig. A-1.

and the other are for the perpendicular direction, where both directions are parallel to each side of the frame. Fig. 4-3 shows the acquired profiles. Here, all the profiles were digitized to keep the JRC determination process to be compatible with the method introduced in section 2.5. They were

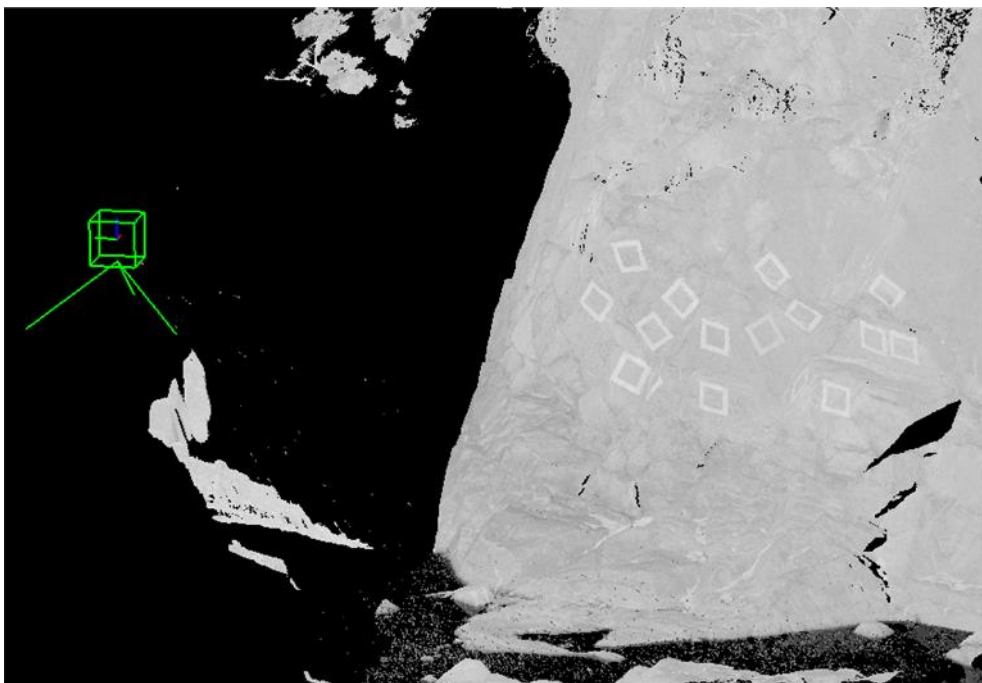


Figure 4–4. Point cloud of the outcrop visualized by CloudCompare.

scanned into image files and then turned into the numeric data using a software, GetData Graph Digitizer. This program automatically recognizes graphs and digitizes them into (x, y) coordinates with a regular sampling interval (Δx in Eq. 2–8). Since the profiles are 15 cm long while reference JRC profiles are 10 cm long, only the middle 10 cm was extracted and used. And then, Eq. (2–8) and the third equation of (2–17) were employed to calculate their Z_2 and JRC. Three JRC values in one direction were averaged to be the representative value for that direction, and thus, true JRC_x and JRC_y of 17 surfaces were obtained.

On the other hand, point cloud from Faro Focus S 350+ was also processed. Firstly, the point cloud was moved to personal computer in the form of PTX format. The file contains not only the point cloud information (xyz-coordinates), but also the scanner's location and intensity measurements of each point. To handle the data, an open source software, CloudCompare, was utilized. CloudCompare automatically shows the scanner and the point

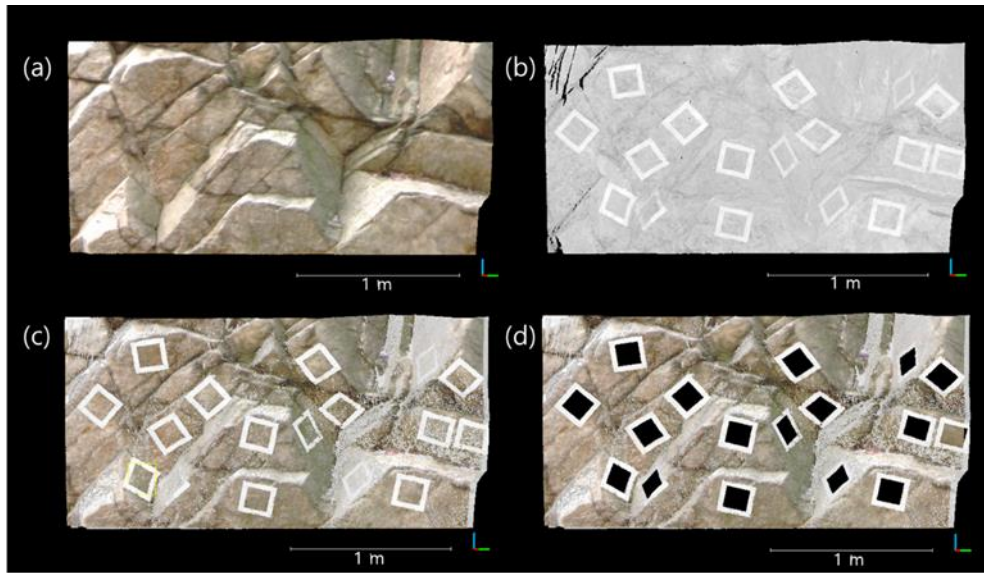


Figure 4–5. Matching two different point clouds of the same object. (a): Point cloud from Faro Focus S 350, (b): Point cloud from Faro Focus S 350+, (c): (a) and (b) after registration using ICP, (d): Remaining point clouds after the targets were cropped.

cloud which is colored with respect to the intensity values when we open a PTX file. Point cloud of the outcrop visualized in CloudCompare is shown in Fig. 4–4. It was easy to recognize the paper frames since they have the reflectance different from the rock. At the same time, point cloud from Faro Focus S 350 was also visualized as shown in Fig. 4–5(a). Here, the point cloud is colored by RGB as color mode was set when it was scanned. According to Lee (2020), the scanner was located at 10 m in front of the rock. As shown in Fig. 4–5, two point clouds from different devices were matched by using Iterative Closest Point (ICP) registration algorithm which is a plugin tool of CloudCompare. After that, surface inside the frames was cut with the segment tool. Here, data from Faro Focus S 350 did not fully include one of the 17 surfaces as shown in Fig. 4–5–(d). Therefore, 17 and 16 surfaces were acquired from Faro Focus S 350+ and 350 data, respectively. Sequentially, the surfaces were rotated and translated to lie on xy-plane, their sides being parallel to x- or y-axis, and cut to have

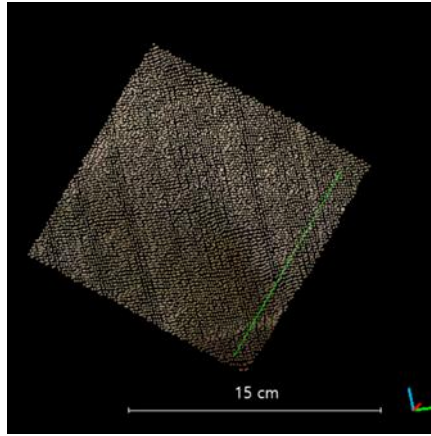


Figure 4–6. Line drawn to be parallel to a side of the surface.

$10 \times 10 \text{ cm}^2$ area by following process:

- ① Draw a line parallel to a side of the surface as shown in Fig. 4–6 using the built-in function of CloudCompare, polyline.
- ② Conduct Principal Component Analysis (PCA) on the surface.
- ③ Obtain the rotation matrix which makes the third principal component (which is equal to the normal vector of best-fit plane of the surface) to match with z-axis direction.
- ④ Rotate the surface and the line using the matrix.
- ⑤ Obtain another rotation matrix which makes the projection of the line on xy-plane to match with x-axis direction.
- ⑥ Rotate the surface using the second matrix.
- ⑦ Scale the surface in centimeter unit and crop the middle $10 \times 10 \text{ cm}^2$ area.
- ⑧ Translate the surface in the way that the mean coordinate of the points to be $[x, y, z] = [5, 5, 0]$.

Figures of all the resultant surfaces are shown in Table A–1, Appendix A. By comparing the figures in the table, we can see that the data from Faro Focus S 350 have more noise than those from Faro Focus S 350+.

Point clouds in Table A–1 were labeled with JRC_x which had been measured by hand. Same with the process in section 3.7, data were augmented by reflecting the surfaces across $y=x$ and labeling with the corresponding JRC_x (which used to be JRC_y before reflection). Therefore, total 34 and 32 surfaces of Faro Focus S 350+ and 350 were obtained to be the test dataset. Since the surfaces had 3 ~ 4,000 points on average, 2,048 points were picked randomly from each surface to make the number of points same with the training data. Here, process of picking points were repeated for 2,048 times to make 2,048 different data from one surface. In this way, model can carry out JRC estimation 2,048 times for just one surface so that the prediction becomes more reliable by averaging all the estimated values.

Table 4–1. Incidence angle and distance of surfaces from Faro Focus S 350+. Index of each surface is shown in Fig. A–1, Appendix A.

Surface	Incidence angle, °	Distance, m	Surface	Incidence angle, °	Distance, m
1	33.05	9.42	10	59.56	9.73
2	40.06	9.58	11	29.23	9.46
3	34.70	9.56	12	27.55	9.48
4	53.58	9.53	13	48.07	9.51
5	23.14	9.41	14	49.52	9.56
6	25.96	9.56	15	40.14	9.68
7	24.33	9.77	16	21.65	9.80
8	31.71	9.71	17	31.29	9.52
9	23.02	9.57			

In the meanwhile, incidence angle and distance of the obtained surfaces have to be looked into since they have been restricted to be less than 45° and between 8 and 12 m, respectively in section 3.6. Based on the location of the device recorded in PTX file from Faro Focus S 350+, incidence angle and distance of the surfaces from Faro Focus S 350+ were calculated and the results are shown in Table 4–1. Here, we can see that the incidence angle of surface 4, 10, 13 and 14 exceeds 45° . Nevertheless, they were not excluded since the amount of excess is not that large and they consist of more than 2,048 points. Unfortunately, device location is not recorded in the data from Faro Focus S 350. However, it is presumed that both devices were installed at similar location considering the point density of each surface. Therefore, all the obtained surfaces will be used without any exception.

4.3. Training procedure

The original code of PointNet was obtained from a Github page^①, which is shared by Qi et al. (2017). It was modified to solve a certain problem, to estimate JRC_x of input point clouds. Here, T-nets in the original structure, which are for keeping the invariance under affine transformation, were not employed for the following reasons:

- ① Position of the surfaces are already aligned.
- ② Since joint roughness is usually anisotropic, estimated JRC has to be differ as the joint surface rotate.

The output size of the last fully-connected layer was changed into 1 to print

^① <https://github.com/charlesq34/pointnet>

out only JRC_x , and the size of input data was fixed as $2,048 \times 3$. Also, the objective function was changed to mean squared error which is appropriate for solving regression problems.

After the modification, PointNet was trained to predict JRC_x of the training data and training was stopped when the minimum prediction loss on 8 surfaces arbitrarily selected from the test dataset was achieved.

4.4. Test results and comparative analysis

1) Test results of existing method and trained ANN

For a comparative analysis, an existing method to calculate JRC using TLS was utilized before testing the trained ANN, which has been introduced in section 3.3. Detailed procedure is as follows:

- ① Convert the surfaces on TLS scan data into mesh using Delaunay triangulation.
- ② Obtain roughness profiles parallel to x-axis direction from each surface by cross-sectioning the mesh as shown in Fig. 4–7.
- ③ Calculate JRC of each profile using Z_2 -JRC relationship (Eq. 2–8 and 2–17).

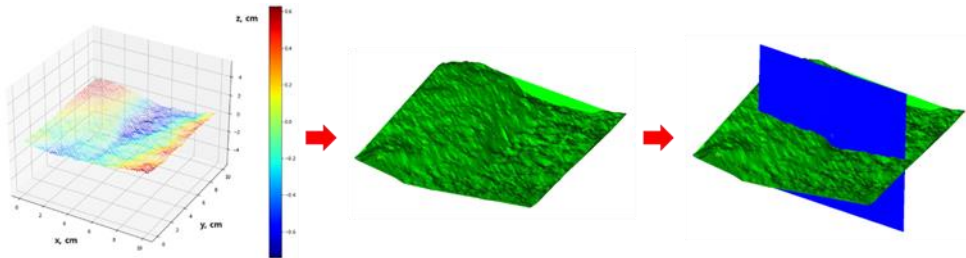


Figure 4–7. Acquisition of roughness profile from TLS scan data using existing method used in Kemeny and Turner (2008) and Marsch et al. (2020).

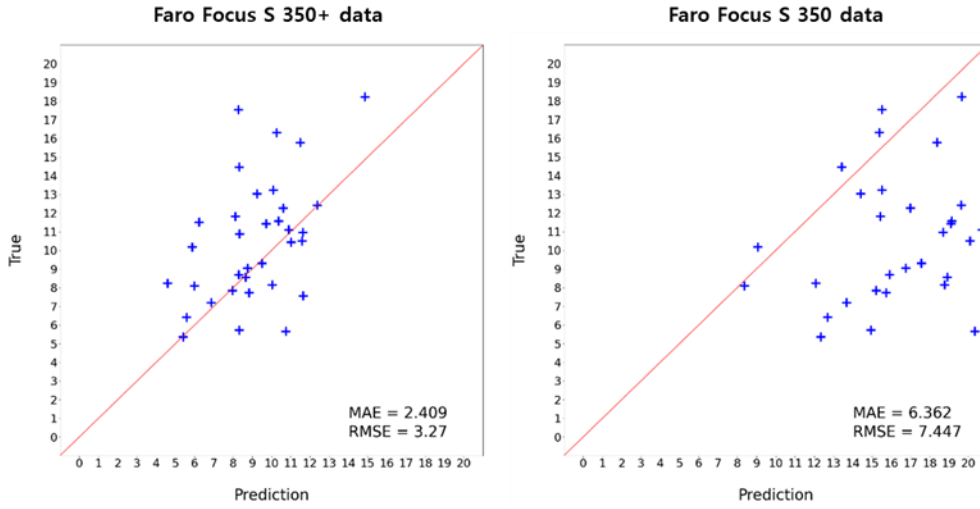


Figure 4–8. Results of the JRC_x measurement on test dataset using the existing method. Left figure shows the result on surfaces from Faro Focus S 350+, and right one shows the result on surfaces from Faro Focus S 350.

Horizontal and vertical axes of each figure represent model' s JRC_x prediction and hand-measured JRC_x , respectively.

- ④ Get JRC_x of each surface by averaging JRC values from its profiles.

JRC_x of the 66 surfaces of test dataset (34 surfaces from Faro Focus S 350+ and 32 surfaces from Faro Focus S 350) was measured following the above process and the results are shown in Fig. 4–8. Here, we can see that this method works quite well on the Faro Focus S 350+ data while

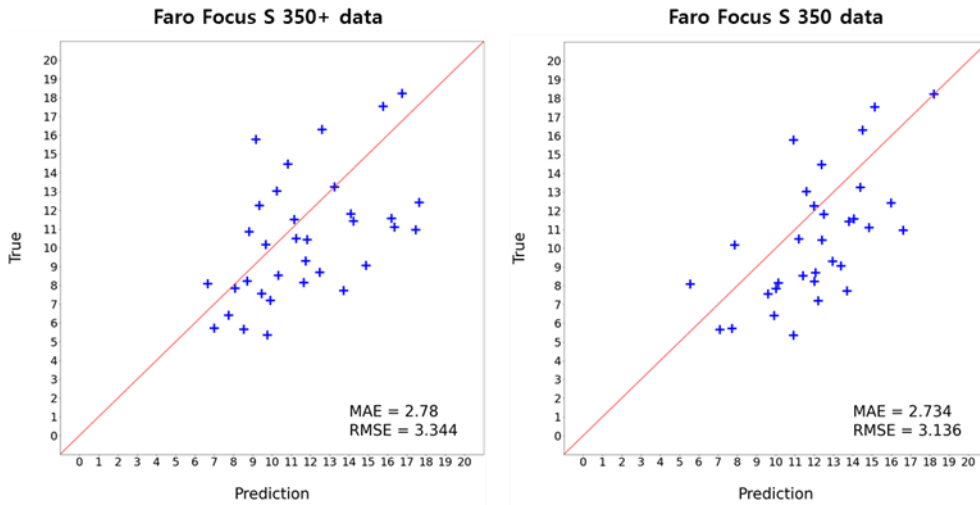


Figure 4–9. Results of the ANN' s JRC_x estimation on test dataset.

significantly overestimating JRC_x of the Faro Focus S 350 data containing more noise.

Trained ANN also carried out estimating JRC_x on 66 surfaces of the test data. As shown in Fig. 4–9, the model estimated JRC_x of point clouds from both TLSs with the average error of JRC 2 ~ 3.

2) Discussion

Based on the test results of existing method shown in Fig. 4–8, it seems that it works well on data from Faro Focus S 350+ while significant overestimating JRC on data from Faro Focus S 350. Given that the data from Faro Focus S 350+ and S 350 are exactly the same surfaces, it appears that the significant overestimation on the latter occurs since Faro Focus S 350 has noise level slightly larger than S 350+. That means the noise existing in TLS scan data can seriously affect JRC estimation and the existing method is not reliable when it is applied on noisy data.

Nevertheless, it can be thought that it is enough to use the existing method to measure JRC when we use a TLS with less amount of noise such as Faro Focus S 350+. But it must be considered that the amount of noise is not a fixed value for a device. Referring to Eq. (3–3), many other factors like surface reflectivity and atmospheric condition will affect the noise level, leading to misestimation of JRC.

On the other hand, based on the test results shown in Fig. 4–9, it is shown that the trained ANN can estimate JRC_x of rock joints scanned by two different TLS devices, Faro Focus S 350+ and 350, with mean absolute error of 2.7. Considering that each of the reference profiles for JRC visual comparison covers JRC range of 2 (Fig. 2–1), this amount of error can be

seen as tolerable. It is remarkable that the trained ANN can estimate JRC regardless of the difference in noise level.

However, there are some limitations to be mentioned. First, the trained ANN was tested only on one granite exposure which has been quite weathered. As there are so many other types of discontinuities (e.g. fault, bedding plane) having so many different surfaces characteristics (e.g. roughness, weathering), a lot more validation is required to confirm the applicability of the trained ANN on JRC estimation. Also, the model used in this thesis is trained based on the noise of specific TLS devices, Faro focus S 350+ and 350, so the applicability on data from other types of TLS has not been looked into at all.

One may think that the procedure for utilizing the trained ANN is too complicated and time-consuming. But there are several steps that will not be included when the trained ANN is used only for estimation, not for validation. The procedure to use the trained ANN for estimation can be summarized as follows:

- ① Locate the TLS to be 8 ~ 12 m apart from the target joint and try to make the incidence angle of the laser on the target smaller than 45°.
- ② Conduct scanning.
- ③ Using CloudCompare, crop the joint of interest to be larger than 10×10 cm². Here, let one of their sides to be parallel to the probable shear direction so that the JRC in shear direction could be estimated.
- ④ Align and cut the cropped surface making the shear direction to be x-axis direction following the procedure introduced in section 4.2.
- ⑤ Pick 2,048 points randomly.
- ⑥ Input the processed data in the trained ANN.

4.5. How to deal with scale effect

As mentioned in section 2.3, JRC has scale effect and there are two different ways available to deal with the scale effect using only TLS scan data; One is amplitude–length method (a/L method) and the other is scaling JRC using reduction equation (Eq. 2–15). In this section, both methods are tested on the point cloud from Faro Focus S 350 which is shown in Fig. 4–5(a). 11 joints were selected from the point cloud as shown in Fig. B–1 of Appendix B and their scaled JRC (JRC_n) was measured using following process.

- ① Amplitude–length method: Joint surfaces containing the lines in Fig. B–1 were cropped and meshed using Delaunay triangulation. Large–scale roughness profiles of the surfaces were obtained by projecting the lines on the meshes in normal direction. After each profiles were aligned so that their best–fit line is horizontal, the maximum amplitude (a) and joint length (L) were measured. Finally, JRC_n of each joint was calculated using Eq. (2–16) and weighted averaging.
- ② Using reduction equation on JRC estimation of trained ANN (JRC_{ANN}): 3 surfaces of $10 \times 10 \text{ cm}^2$ were obtained from each of the 11 joints. After they were aligned such that the x–axis direction is parallel to the line drawn in Fig. B–1, the trained ANN estimated their JRC_x . As a result, 3 JRC values were obtained and they were scaled with respect to joint length using Eq. (2–15). Finally, JRC_n was derived by averaging those 3 values.

Results of the above process are shown in Table 4–2. In this table, there is an additional column representing whether the joint has large–scale undulation or not. As mentioned in section 2.3, Eq. (2–15) does not work well on joint samples with dissimilar roughness on small and large scales. Therefore, joints having large–scale undulation were checked by observing

Table 4–2. JRC_n estimated with two different methods.

Joint	Length, m	Large– scale undulation	Amplitude / Length (a/L)		ANN + Eq. (2–15)	
			a/L, %	JRC _n	JRC _{ANN}	JRC _n
1	0.775	X	1.663	7.3	7.9	5.6
2	0.528	O	3.437	15.5	9.1	6.5
3	0.348	X	1.596	6.6	12.7	9.2
4	0.534	O	3.930	16.7	15.7	9.2
5	0.399	O	4.627	19.3	12.1	8.7
6	0.445	X	2.328	9.8	6.3	5.2
7	0.319	X	2.080	8.6	10.4	8.2
8	0.326	O	4.681	19.3	11.8	8.9
9	0.424	X	1.312	5.5	5.0	4.2
10	0.402	O	6.343	26.4	16.3	10.3
11	0.481	X	2.754	11.6	13.2	8.7

their roughness profiles shown in Table B–1, Appendix B. Note that it is based on the author’ s personal judgement.

In Table 4–2, it is shown that JRC_n values of the two methods are comparable when the joint does not have large–scale undulation, whereas otherwise, JRC_n of a/L method is much larger than that of the ANN. That means, large–scale undulations existent in large joints are not detected with the small portion of the joints. Therefore, it is recommended to utilize both methods concurrently for large joints to gain information on the large–scale roughness component (waviness). It is also noteworthy that the joints with large–scale undulation are of the same joint set according to Lee (2020).

Chapter 5. Conclusion

In this thesis, a method to estimate JRC of rock exposure using TLS and ANN was suggested, which enables safe and fast assessment of rock mass roughness. TLS can scan rock exposure in distance and convert it into the form of point cloud while the ANN, PointNet, can receive point cloud of rock surface as input and predict its JRC.

The original methods to measure JRC and its utility in Barton–Bandis joint model were summarized. Focusing on the visual comparison method, ways to measure JRC more precisely were reviewed together with issues relevant to JRC measurement such as scale effect and anisotropy.

Purpose of employing the ANN was to deal with noises existing in TLS scan data. In many previous works it was mentioned that it is hard to measure small-scale roughness using TLS due to the existence of noise. The strategy used in this thesis was to make a noise-independent JRC estimator by training the ANN with noise-applied dataset. In this way, it was believed that the ANN will automatically learn how to deal with the noise in TLS scan data.

Since large amount of point cloud of rock joint is needed to train PointNet, a computer code which can generate random rough surfaces were utilized instead of real TLS scan data. This code is based on fractal theory which used to be employed in rock mechanics. Using the code, synthetic point clouds with different characteristics were generated and their JRC values were calculated to label them.

Noise types in TLS scan data that reduce precision were classified into three; range noise, angular noise and mixed-pixel effect. Based on their principles,

an algorithm to simulate them were developed and applied on the generated synthetic rough surfaces. As a result, noise-applied dataset for training PointNet has been made.

Two different TLS devices, Faro Focus S 350+ and Faro Focus S 350, were employed to conduct field scanning on a granite outcrop to make test dataset for validation of trained ANN. For a comparative analysis, an existing method to measure JRC was tested together with the trained ANN. It was shown that the existing method works well on Faro Focus S 350+ data while significant overestimation of JRC occurs on Faro Focus S 350 data since Faro Focus S 350 data contains more noise. From this result, it was found that noise in TLS scan data can induce severe misestimation of JRC. On the other hand, it was shown that the trained ANN can estimate JRC of the test dataset regardless of the noise level with average error of JRC 2 ~ 3.

Given that JRC has scale effect, two different ways to measure JRC of joints larger than the standard size (10 cm) were introduced. One is amplitude-length method and the other is using reduction equation on the estimation of trained ANN. Using those methods, JRC of relatively large-scale (0.3 ~ 1.0 m) joints were estimated using the TLS scan data. The result showed that the estimations from two methods are similar to each other for joints without large-scale undulation while there are significant differences on joints with large-scale undulation. Therefore, it is recommended to use both methods concurrently for large joints.

Results of validation of the trained ANN indicates that it is possible to measure small-scale roughness using TLS in the presence of noise. Yet, the validation was done only on one granite exposure and applicability of the ANN to large-scale joints has not been validated. In addition, since there are various joints having different characteristics (e.g. rock type,

roughness), a lot more tests should be done in the future. It should also be mentioned that the model used in this thesis has been trained based on the noise of specific TLS devices, Faro focus S 350+ and 350, so the applicability on data from other types of TLS has not been looked into.

References

- Babadagli, T., & Develi, K. (2001). On the application of methods used to calculate the fractal dimension of fracture surfaces. *Fractals*, 9(01), 105–128.
- Bandis, S., Lumsden, A., & Barton, N. (1981). Experimental studies of scale effects on the shear behaviour of rock joints. *International Journal of Rock Mechanics and Mining Sciences & Geomechanics Abstracts*, (Vol. 18, No. 1, pp. 1–21). Pergamon.
- Barton, N. (1982a). *Modelling rock joint behavior from in situ block tests: implications for nuclear waste repository design* (Vol. 308). Office of Nuclear Waste Isolation, Battelle Project Management Division.
- Barton, N. (1982b). Shear strength investigations for surface mining. *In Proceedings of the 23rd US Rock Mechanics Symposium* (pp. 178–180).
- Barton, N. R., & Bandis, S. C. (2017). Characterization and modeling of the shear strength, stiffness and hydraulic behavior of rock joints for engineering purposes. *In Rock Mechanics and Engineering* (pp. 3–40). CRC Press.
- Barton, N., Bandis, S., & Bakhtar, K. (1985). Strength, deformation and conductivity coupling of rock joints. *In International journal of rock mechanics and mining sciences & geomechanics abstracts* (Vol. 22, No. 3, pp. 121–140). Pergamon.
- Barton, N., & Choubey, V. (1977). The shear strength of rock joints in theory and practice. *Rock Mechanics*, 10(1), 1–54.
- Bitenc, M., Kieffer, D. S., & Khoshelham, K. (2019). Range versus surface denoising of terrestrial laser scanning data for rock discontinuity roughness estimation. *Rock Mechanics and Rock Engineering*, 52(9),

3103–3117.

Brown, S. R. (1987). Fluid flow through rock joints: the effect of surface roughness. *Journal of Geophysical Research: Solid Earth*, 92(B2), 1337–1347.

Carr, J. R., & Warriner, J. B. (1989). Relationship between the fractal dimension and joint roughness coefficient. *Bulletin of the Association of Engineering Geologists*, 26(2), 253–263.

Chaudhry, S., Salido–Monzú, D., & Wieser, A. (2019). Simulation of 3D laser scanning with phase–based EDM for the prediction of systematic deviations. *Modeling Aspects in Optical Metrology VII*, (Vol.11057, pp. 92–104). SPIE.

Chaudhry, S., Salido–Monzú, D., & Wieser, A. (2021). A modeling approach for predicting the resolution capability in terrestrial laser scanning. *Remote Sensing*, 13(4), 615.

Faro. (2021). *TechSheet Focus Laser Scanner EN*. (https://media.faro.com/-/media/Project/FARO/FARO/FARO/Resources/2_TECH-SHEET/TechSheet_Focus_Laser_Scanner/TechSheet_Focus_Laser_Scanner_EN.pdf?rev=1291d7f5ef814fe99d471dde60321833). Retrieved November 23, 2022.

Fardin, N., Feng, Q., & Stephansson, O. (2004). Application of a new in situ 3D laser scanner to study the scale effect on the rock joint surface roughness. *International Journal of Rock Mechanics and Mining Sciences*, 41(2), 329–335.

Feng, Q., & Röshoff, K. (2015). A survey of 3D laser scanning techniques for application to rock mechanics and rock engineering. In *The ISRM Suggested Methods for Rock Characterization, Testing and Monitoring: 2007–2014* (pp. 265–293). Springer.

Fereshtenejad, S., Kim, J., & Song, J. J. (2021). Experimental Study on

- Shear Mechanism of Rock-Like Material Containing a Single Non-Persistent Rough Joint. *Energies*, 14(4), 987.
- Gigli, G., & Casagli, N. (2011). Semi-automatic extraction of rock mass structural data from high resolution LIDAR point clouds. *International Journal of Rock Mechanics and Mining Sciences*, 48(2), 187–198.
- Grasselli, G., & Egger, P. (2003). Constitutive law for the shear strength of rock joints based on three-dimensional surface parameters. *International Journal of Rock Mechanics and Mining Sciences*, 40(1), 25–40.
- Holst, C., Artz, T., & Kuhlmann, H. (2014). Biased and unbiased estimates based on laser scans of surfaces with unknown deformations. *Journal of Applied Geodesy*, 8(3), 169–184.
- Huang, S., Oelfke, S., & Speck, R. (1992). Applicability of fractal characterization and modelling to rock joint profiles. *International Journal of Rock Mechanics and Mining Sciences & Geomechanics Abstracts*, (Vol. 29, No. 2, pp. 89–98). Pergamon.
- ISRM. (1978). Commission on standardization of laboratory and field tests: Suggested methods for the quantitative description of discontinuities in rock masses. *International Journal of Rock Mechanics Mining Sciences*, 15, 319–368.
- Jacobs, T. D., Junge, T., & Pastewka, L. (2017). Quantitative characterization of surface topography using spectral analysis. *Surface Topography: Metrology and Properties*, 5(1), 013001.
- Jang, H. S., Kang, S. S., & Jang, B. A. (2014). Determination of joint roughness coefficients using roughness parameters. *Rock Mechanics and Rock Engineering*, 47(6), 2061–2073.
- Kanafi, M. M. (2022). *Surface generator: artificial randomly rough surfaces*.

- (<https://www.mathworks.com/matlabcentral/fileexchange/60817-surface-generator-artificial-randomly-rough-surfaces>), MATLAB Central File Exchange. Retrieved October 28, 2022.
- Kemeny, J., & Turner, K. (2008). *Ground-based lidar: rock slope mapping and assessment* (No. FHWA-CFL/TD-08-006). United States. Federal Highway Administration. Central Federal Lands Highway Division.
- Kulatilake, P. H. S. W., Shou, G., Huang, T. H., & Morgan, R. M. (1995). New peak shear strength criteria for anisotropic rock joints. *In International Journal of Rock Mechanics and Mining Sciences & Geomechanics Abstracts* (Vol. 32, No. 7, pp. 673-697). Pergamon.
- Kulatilake, P. H. S. W., Um, J., & Pan, G. (1997). Requirements for accurate estimation of fractal parameters for self-affine roughness profiles using the line scaling method. *Rock mechanics and rock engineering*, 30(4), 181-206.
- Kulatilake, P., & Um, J. (1999). Requirements for accurate quantification of self-affine roughness using the roughness-length method. *International Journal of Rock Mechanics and Mining Sciences*, 36(1), 5-18.
- Lee, Y.-H., Carr, J., Barr, D., & Haas, C. (1990). The fractal dimension as a measure of the roughness of rock discontinuity profiles. *International Journal of Rock Mechanics and Mining Sciences & Geomechanics Abstracts* (Vol. 27, No. 6, pp. 453-464). Pergamon.
- Lee, S. (2020). *Automated Characterization of Rock Mass Discontinuities Using LiDAR Point Cloud*. Graduate School of Seoul National University.
- Maerz, N. H., Franklin, J. A., & Bennett, C. P. (1990). Joint roughness measurement using shadow profilometry. *In International Journal of*

- Rock Mechanics and Mining Sciences & Geomechanics Abstracts*
(Vol. 27, No. 5, pp. 329–343). Pergamon.
- Mandelbrot, B. B. (1982). *The fractal geometry of nature* (Vol. 1). WH Freeman New York.
- Marsch, K., Wujanz, D., & Fernandez–Steege, T. M. (2020). On the usability of different optical measuring techniques for joint roughness evaluation. *Bulletin of Engineering Geology and The Environment*, 79(2), 811–830.
- Marshall, G. F., & Stutz, G. E. (2012). *Handbook of optical and laser scanning* (p. 788). Taylor & Francis.
- Muralikrishnan, B. (2021). Performance evaluation of terrestrial laser scanners—A review. *Measurement Science and Technology*, 32(7), 072001.
- Odling, N. (1994). Natural fracture profiles, fractal dimension and joint roughness coefficients. *Rock Mechanics and Rock Engineering*, 27(3), 135–153.
- Photonik, V., & Sandner, M. P. *Optical measurement of partially specular surfaces by combining pattern projection and deflectometry techniques*.
- Qi, C. R., Su, H., Mo, K., & Guibas, L. J. (2017). Pointnet: Deep learning on point sets for 3d classification and segmentation. *Proceedings of the IEEE Conference on Computer Vision and Pattern Recognition* (pp. 652–660).
- Reshetyuk, Y. (2009). *Self-calibration and direct georeferencing in terrestrial laser scanning* (Doctoral dissertation, KTH).
- Schmitz, B., Holst, C., Medic, T., Lichti, D. D., & Kuhlmann, H. (2019). How to efficiently determine the range precision of 3D terrestrial laser scanners. *Sensors*, 19(6), 1466.

- Soudarissanane, S. S. (2016). *The geometry of terrestrial laser scanning: identification of errors, modeling and mitigation of scanning geometry*.
- Soudarissanane, S., Lindenbergh, R., Menenti, M., & Teunissen, P. (2011). Scanning geometry: Influencing factor on the quality of terrestrial laser scanning points. *Isprs Journal of Photogrammetry and Remote Sensing*, 66(4), 389–399.
- Tatone, B. S. (2009). *Quantitative characterization of natural rock discontinuity roughness in-situ and in the laboratory*. University of Toronto Toronto.
- Tatone, B. S., & Grasselli, G. (2009). A method to evaluate the three-dimensional roughness of fracture surfaces in brittle geomaterials. *Review of Scientific Instruments*, 80(12), 125110.
- Tatone, B. S., & Grasselli, G. (2010). A new 2D discontinuity roughness parameter and its correlation with JRC. *International Journal of Rock Mechanics and Mining Sciences*, 47(8), 1391–1400.
- Tse, R., & Cruden, D. (1979). Estimating joint roughness coefficients. *International Journal of Rock Mechanics and Mining Sciences & Geomechanics Abstracts* (Vol. 16, No. 5, pp. 303–307). Pergamon.
- Wang, Q., Sohn, H., & Cheng, J. C. (2016). Development of a mixed pixel filter for improved dimension estimation using AMCW laser scanner. *Isprs Journal of Photogrammetry and Remote Sensing*, 119, 246–258.
- Wujanz, D., Burger, M., Mettenleiter, M., & Neitzel, F. (2017). An intensity-based stochastic model for terrestrial laser scanners. *Isprs Journal of Photogrammetry and Remote Sensing*, 125, 146–155.
- Yu, X., & Vayssade, B. (1991). Joint profiles and their roughness parameters. *International Journal of Rock Mechanics and Mining Sciences &*

Appendix A. Figures of test data

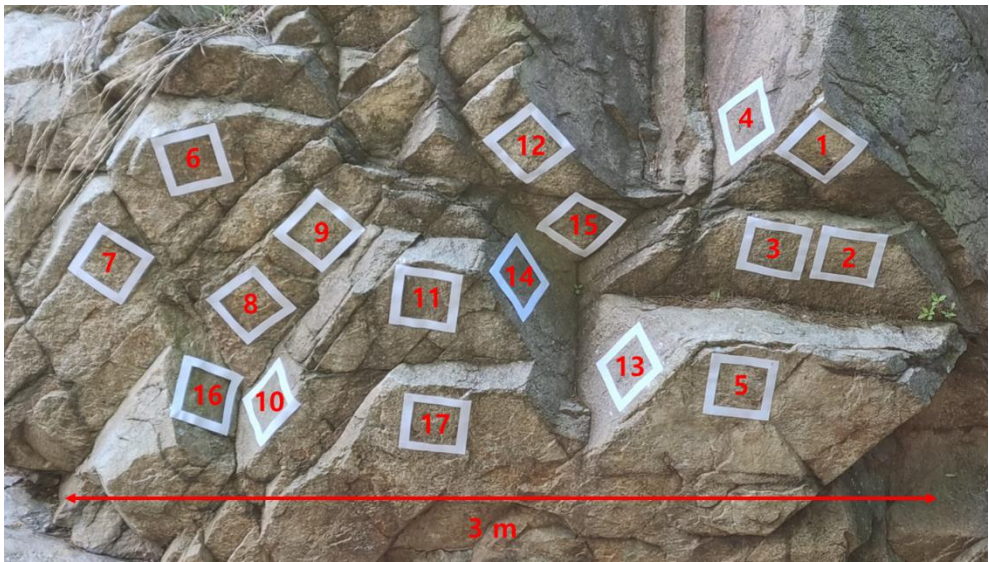
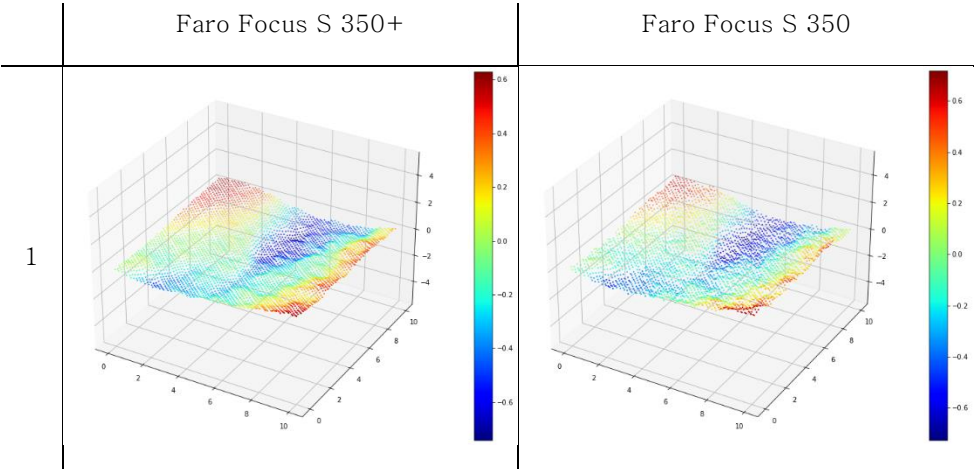
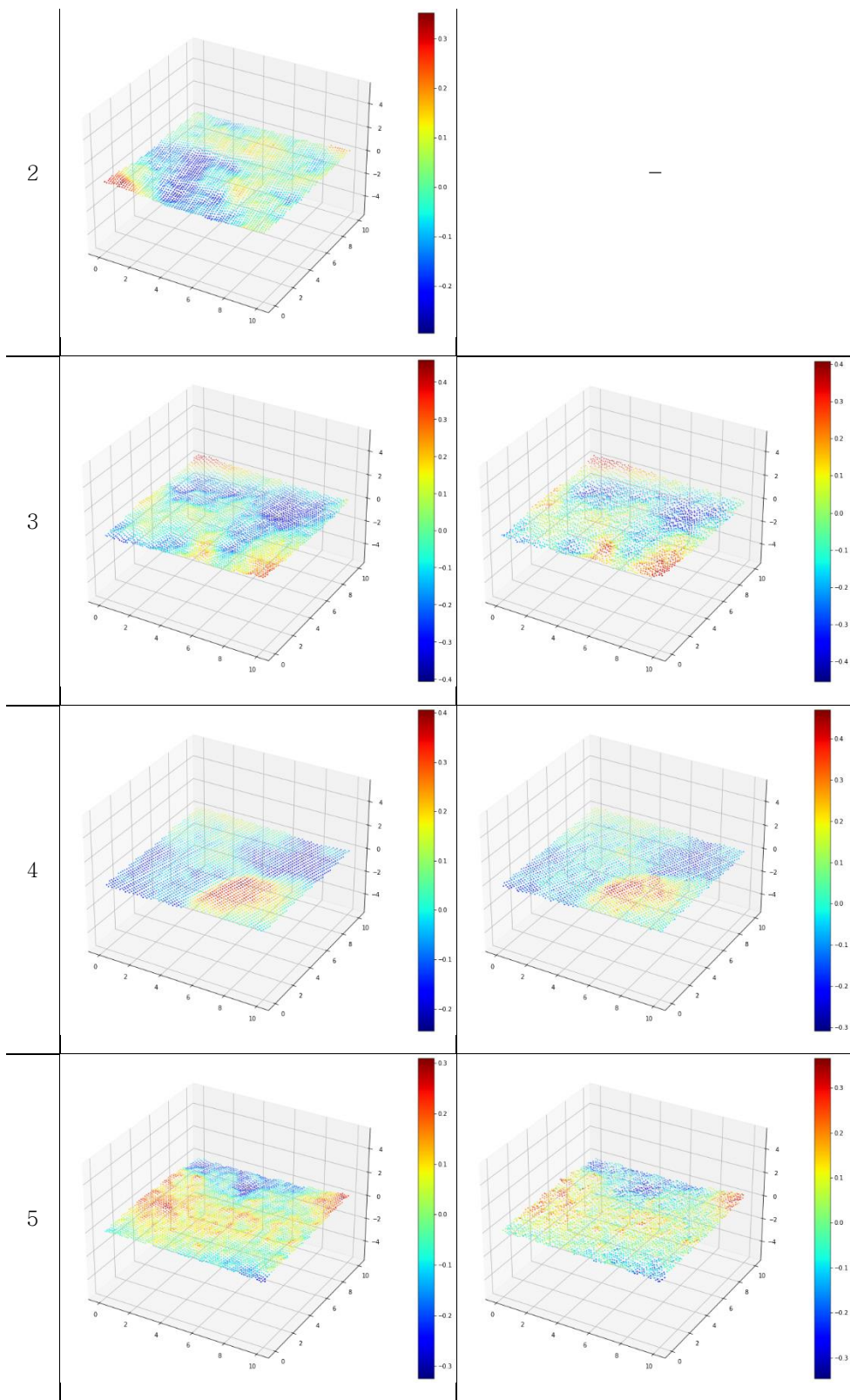
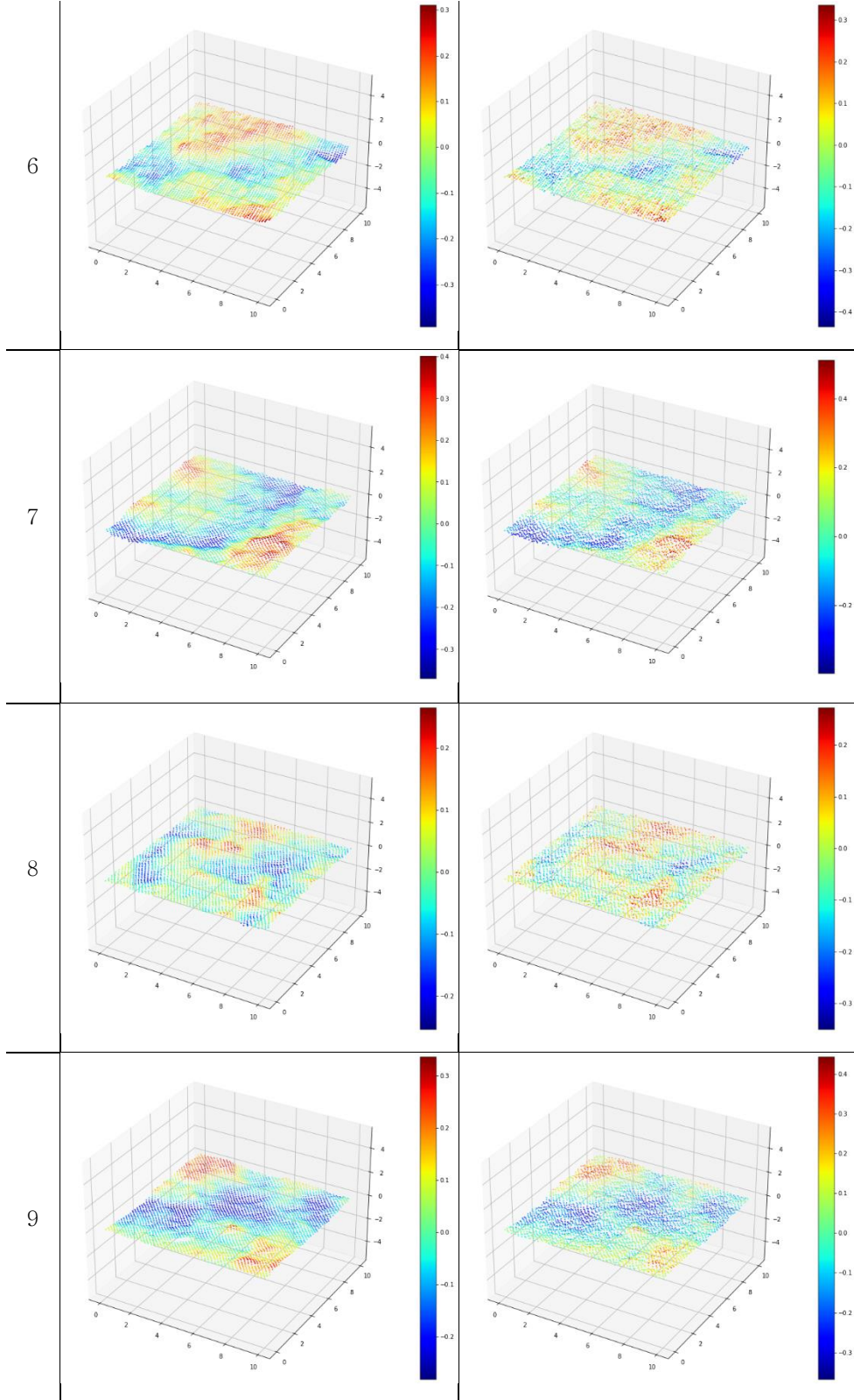


Figure A-1. Index of test data.

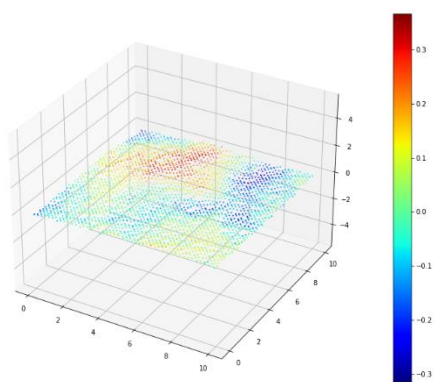
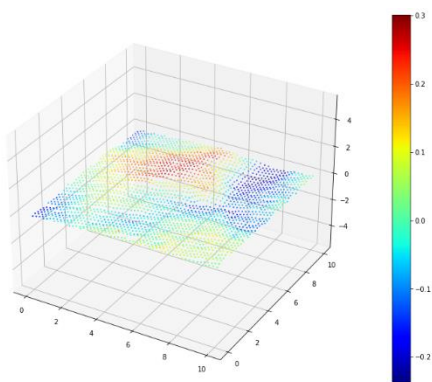
Table A-1. 3D plot of test data shown in Fig. A-1. First, second and third column represent data index, corresponding data scanned by Faro Focus S 350+ and corresponding data scanned by Faro Focus S 350, respectively. Here, point cloud from Faro Focus S 350 did not contain surface #2. Digits in the plots are in centimeter unit.



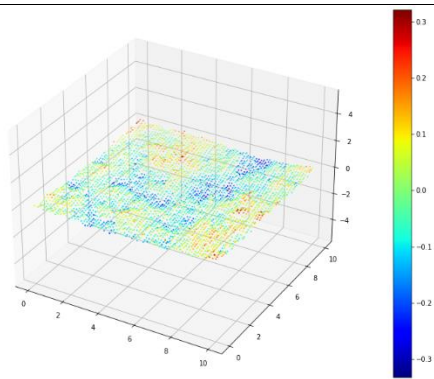
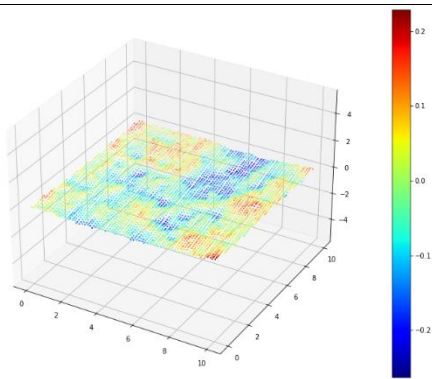




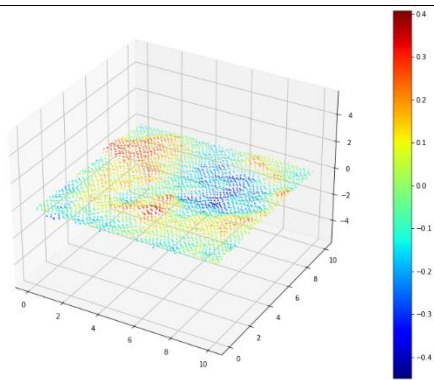
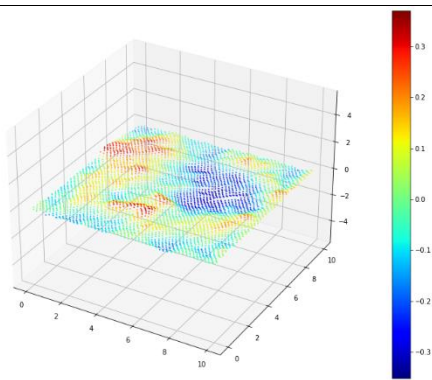
10



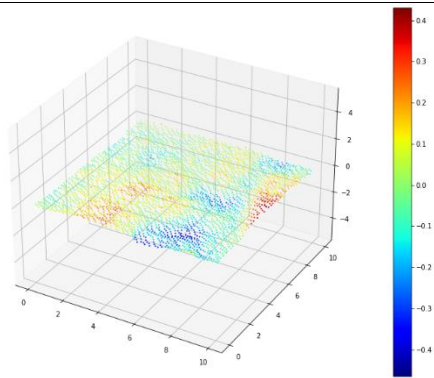
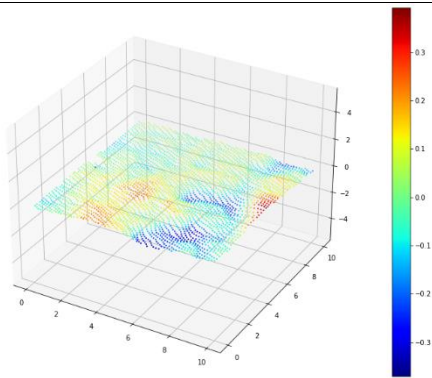
11



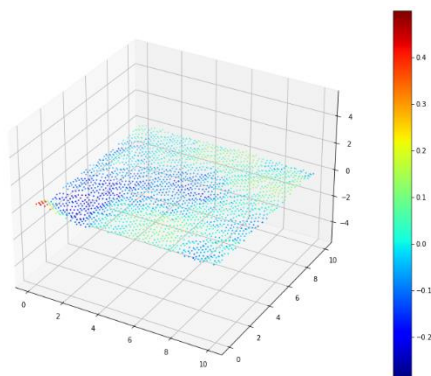
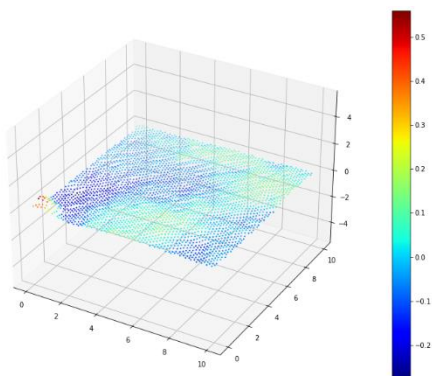
12



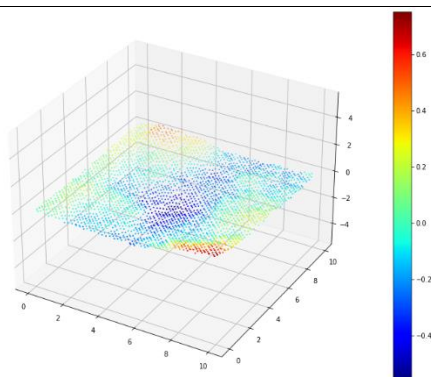
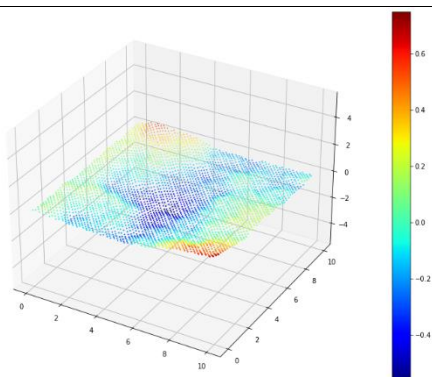
13



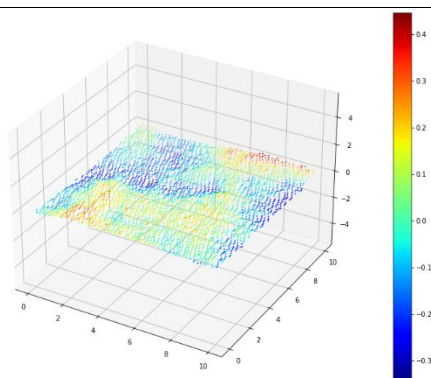
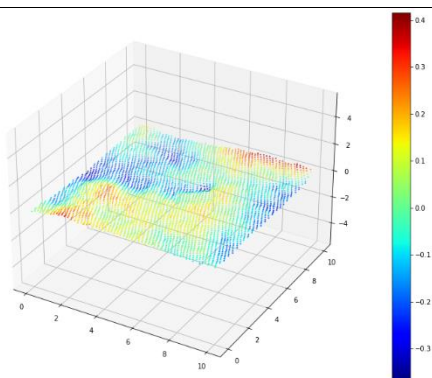
14



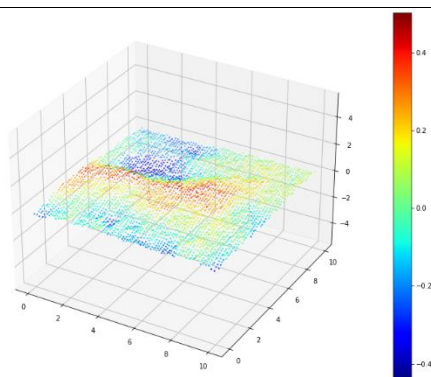
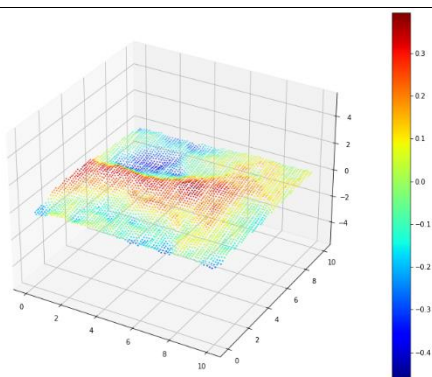
15



16



17



Appendix B. Large scale roughness profiles

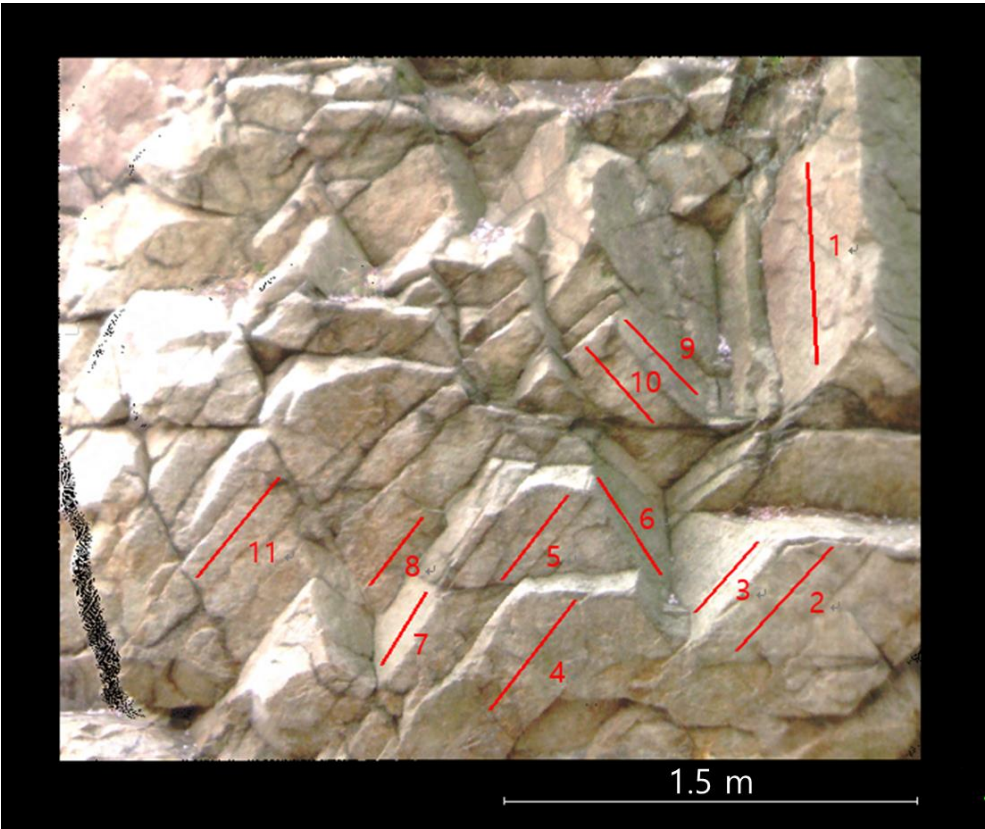
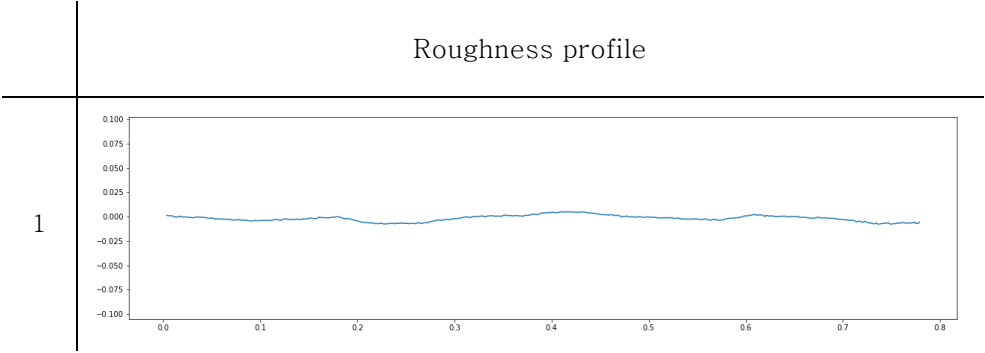
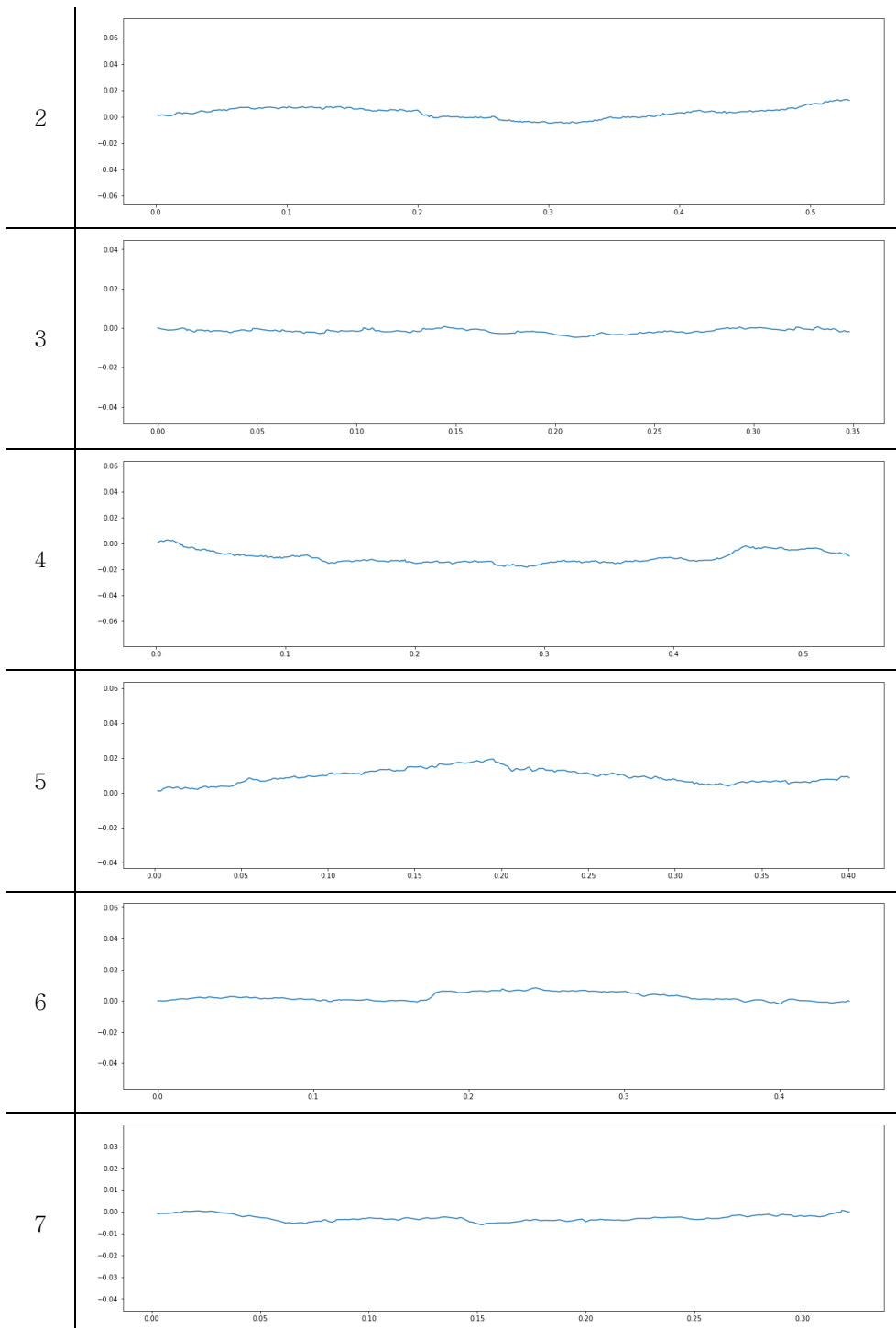


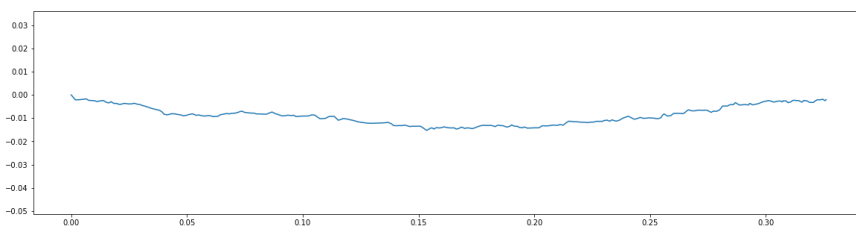
Figure B-1. Index of the profiles.

Table B-1. Plots of roughness profiles in Fig. B-1. First column represents the index. Digits in the plots are in meter unit.

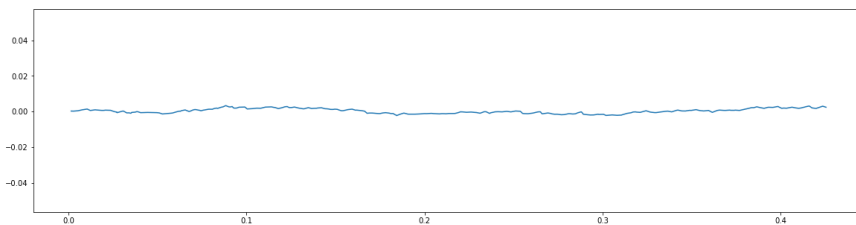




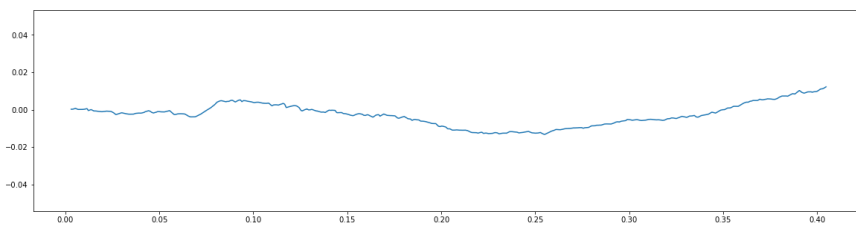
8



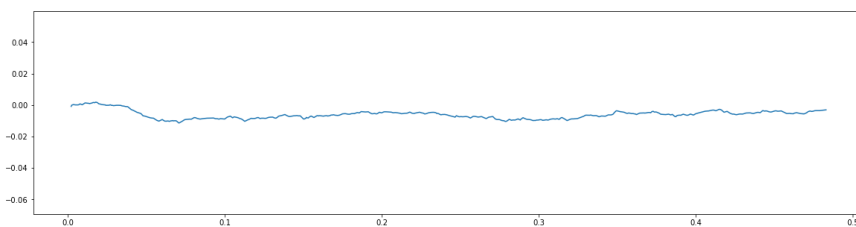
9



10



11



초 록

절리 거칠기 지수(Joint Roughness Coefficient; JRC)는 Barton-Bandis 절리 모델에서 암반 불연속면의 거칠기 정도를 나타내는 인자이다. 이는 원하는 불연속면으로부터 취득한 거칠기 프로파일을 기준 프로파일과 시각적으로 비교함으로써 측정할 수 있다. 이 방법은 절리 시료를 취득하여 실험실 또는 현장 시험을 실시하는 것보다는 훨씬 편리하지만 경우에 따라 실시하는 데 오랜 시간이 필요하거나 위험할 수 있다. 본 논문에서는 이러한 문제를 해결하기 위하여 지상레이저스캐너 (Terrestrial Laser Scanner; TLS)를 이용하여 빠르고 안전하게 절리 거칠기 지수를 산정하는 방법을 제시하고자 한다. 지상레이저스캐너를 이용하여 암반 노출면의 삼차원 점군을 원거리에서 취득하고 점군 내 불연속면들의 절리 거칠기 지수를 추정할 것이다.

몇몇의 기존 연구들에 따르면 지상레이저스캐너를 이용하여 작은 규모의 거칠기를 산정하는 것은 데이터에 존재하는 노이즈 때문에 매우 어렵다고 한다. 본 논문에서는 이를 해결하기 위한 전략으로 3차원 점군을 위한 인공신경망을 사용하고자 하였다. 사용된 인공신경망은 불연속면의 점군을 입력받아 그것의 절리 거칠기 지수를 예측할 수 있다. 해당 인공신경망을 노이즈를 포함하는 다량의 점군 데이터셋으로 학습시킴으로써 인공신경망이 노이즈의 존재와 상관없이 점군의 절리 거칠기 지수를 산정하는 방법을 학습하도록 하였다. 지상레이저스캐너를 이용하여 실제 데이터셋을 구축하는 것이 불가능했기 때문에 실제 암반 스캔 자료 대신 프랙탈 이론을 기반으로 한 알고리즘을 사용하여 가상의 거친 표면 점군 데이터셋을 생성하였다. 각 표면을 해당 표면의 절리 거칠기 지수로 라벨링한 후, 실제 스캔 자료를 모사하기 위하여 표면들에 지상레이저스캐너의 노이즈를 인공적으로 입혀주었다.

인공신경망은 가상 학습 데이터셋으로 학습된 후 실제 암반 스캔 자료에 대하여 검증되었다. 그 결과 학습된 인공신경망은 스캔 데이터 내에 존재하는 노이즈의 수준과 상관 없이 절리 표면의 절리 거칠기 지수를 산정할 수 있었다. 반면에 기존에 존재하던 방법으로 같은 데이터에 대하여 절리 거칠기 지수

산정을 시도하였을 때에는 노이즈가 클 경우 예측이 크게 잘못됨을 확인하였다. 추가적으로, 절리 거칠기 지수가 가지는 크기 효과에 대응하는 방법들 또한 제시되었다.

주요어 : 절리 거칠기 지수, 지상레이저스캐너, 인공신경망, 암석, 점군, 라이다

학 번 : 2021-26971